IR WINDOW STUDIES

Ferdinand Kroger, et al

University of Southern California

Prepared for:

Air Force Cambridge Research Laboratories
Defense Advanced Research Projects Agency

15 December 1973

UNCLASSIFIED
Security Classification

AD-783331

DOCUMENT CONTROL DATA - R & D

(Security classification of title, body of abstract and indexing annotation must be entered when the overall report is classified)

1. ORIGINATING ACTIVITY *(Corporate author)*
University of Southern California
Electronic Sciences Laboratory
Los Angeles, California 90007

2a. REPORT SECURITY CLASSIFICATION
UNCLASSIFIED

2b. GROUP

3. REPORT TITLE
IR WINDOW STUDIES

4. DESCRIPTIVE NOTES *(Type of report and inclusive dates)*
Scientific Interim.

5. AUTHOR(S) *(First name, middle initial, last name)*
Ferdinand Kroger
John H. Marburger

6. REPORT DATE	7a. TOTAL NO. OF PAGES	7b. NO. OF REFS
15 December 1973	88 89	29

8a. CONTRACT OR GRANT NO	9a. ORIGINATOR'S REPORT NUMBER(S)
F19628-72-C-0275	
b. PROJECT, XX Task, Work Unit Nos. 2055 n/a n/a	Quarterly Technical Report No. 6
c. DoD Element 61101D	9b. OTHER REPORT NO(S) *(Any other numbers that may be assigned this report)*
d. DoD Subelement n/a	AFCRL-TR-74-0060

10. DISTRIBUTION STATEMENT
A-Approved for public release; distribution unlimited

11. SUPPLEMENTARY NOTES	12. SPONSORING MILITARY ACTIVITY
This research was supported by the Defense Advanced Research Projects Agency.	Air Force Cambridge Research Laboratories (LQ) L. G. Hanscom Field Bedford, Massachusetts 01730

13. ABSTRACT

The lowest absorption at 10.6μ found with GaAs grown from the melt has temperature dependence expected for multiphonon absorption. GaAs made by chemical transport showed a high 10.6μ absorption due to inclusions. The previously reported value for the dielectric constant of GaAs has to be revised to E = 13.6. Diffuse streaks in the diffraction pattern of GaAs was attributed to diffuse thermal scattering of electrons at acoustic phonons. Slip in GaAs occurs on {111} <1$\bar{1}$0>. Hardness of GaAs is increased by tetragonal defects.

A method to determine oxygen in GaAs with a sensitivity of $5 \times 10^{16} cm^{-3}$ or 0.2 to 1 × a monatomic layer of O was developed.

In GaAs doped with silicon, O present is a concentration < 2 × that of Si, cannot be determined due to the stability of SiO_2.

The theory for thermal lensing is presented in modified form. A method for the determination of mechanism of multiphonon absorption is proposed.

DD FORM 1 NOV 65 1473 (PAGE 1)
0102-014-6600

UNCLASSIFIED
Security Classification

14 KEY WORDS	LINK A		LINK B		LINK C	
	ROLE	WT	ROLE	WT	ROLE	WT
IR Windows						
Alkali Halides						
III-V Semiconductors						
II-VI Semiconductors						
Thermal Lensing						
IR Absorption						

IR WINDOW STUDIES

F. A. Kröger and John H. Marburger

Contract No. F19628-72-C-0275

Quarterly Technical Report No. 6
15 December 1973

Contract Monitor: Alfred Kahan
Solid State Sciences Laboratory

Approved for public release; distribution unlimited.

Prepared for the Defense Advanced Research Projects Agency

ARPA Order No. 2055, as Monitored by

AIR FORCE CAMBRIDGE RESEARCH LABORATORIES
AIR FORCE SYSTEMS COMMAND
UNITED STATES AIR FORCE
BEDFORD, MASSACHUSETTS 01730

ABSTRACT

The theory of thermal lensing is reviewed and presented from a different viewpoint. A method to determine the contributions of various processes to multiphonon absorption is proposed.

For GaAs, the lowest 10.6μ absorptions found have a weak temperature dependence corresponding to theoretical predictions for multiphonon absorption. However, other mechanisms might give the same dependence. Layers of GaAs up to 2mm thick have been made by chemical vapor transport. The layers had inclusions, however, and the high 10.6μ absorption (4×10^{-2} cm^{-1} or larger) probably result from these. Using a newly developed method for oxygen detection with a sensitivity limit of $5 \times 10^{16} cm^{-3}$ or 0.2 to 1 × a monolayer of oxygen show $\simeq 10^{18} cm^{-3}$ O in GaAs-Te. In GaAs-Si, an oxygen content below the Si content cannot be determined. Repeated dielectric constant measurements on GaAs give $\varepsilon = 13.6$. Diffuse streaks in the diffraction pattern of GaAs are attributed to thermal diffuse scattering of electrons at acoustic phonons. Slip in GaAs occurs on {111} $\langle 1\bar{1}0 \rangle$. The hardness of GaAs is increased by tetragonal defects. Hot pressing of CdTe in presence of Cd(ℓ) still gives problems.

KBr with a 10.6μ absorption of $1.1 \times 10^{-3} cm^{-1}$ has been grown.

A TEA laser for damage studies is being assembled.

CONTENTS

1. INTRODUCTION

The format of this report follows closely that of the first quarterly report in which projects are identified by codes keyed to the contract work statement.

The various categories are briefly:

a) Crystal growth
b) Polycrystalline window fabrication
c) Mechanical properties of window materials
d) Window material defect characterization
e) Theory of residual IR optical absorption
f) Absorption measurement techniques
g) Theoretical evaluation of optical performances of windows

a.1 Concentrations of Oxygen in Selected GaAs Samples

P. S. Vijaykumar and J. M. Whelan

The previous report described the determintation of the oxygen concentration - fugacity relationship in Ga solutions for oxygen atomic fractions below 10^{-7}. This information and the measured changes in oxygen fugacities before and after dissolving known amounts of GaAs in Ga solutions have been combined to estimate the oxygen contents of selected GaAs samples. The apparatus has also been previously described. Fugacities are determined from the emf's of reverisble (or nearly so) cells using calcia stabilized zirconia as the oxygen conducting electrolyte. Since the oxygen fugacities are small, they may be described in terms of the equivalent molecular oxygen pressures, P_{O_2} in equilibrium with the Ga solution at the zirconia surface and the reference oxygen pressure, P_{O_2R} in equilibrating H_2O vapor at a partial pressure corresponding to its vapor pressure at 0°C with H_2 at one atomosphere, i.e. 6×10^{-3} atm. The relationship between the emf (assumed to be reversible) and these pressures is

$$\text{emf} = \frac{RT}{2F} \ln\left(\frac{P_{O_2}}{P_{O_2R}}\right)^{1/2}$$

Alternately the oxygen fugacity in the Ga may be related to the equivalent partial pressure of H_2O in 1 atom of H_2:

$$P_{H_2O} = 6 \times 10^{-3}\left(\frac{P_{O_2}}{P_{O_2R}}\right)^{1/2}$$

A GaAs wafer which had a portion of its surface implanted with high energy oxygen ions was selected as a standard for checking the accuracy of the method. Figure A shows the variation with time of $(P_{O_2}/P_{O_2R})^{1/2}$ before and after immersing the implanted sample in the Ga solution at t = 0. Transit effects associated with oxygen gradients in the Ga solutions upon dissolution of the sample were minimized by extrapolation of the long term drift back to the time the sample was immersed. Using this extrapolation figure, the amount of oxygen in the melt was 6×10^{15} atoms. This is to be compared with 3×10^{15} atoms added, estimated from the amount of implanted GaAs dissolved by the Ga solution. Unfortunately, the latter estimate was complicated by the dissolution of the implanted region occuring only at its edges. The majority of the implanted surface was not wetted by the Ga. Several explanations have been

advanced, the ones considered most likely are:

1) the implanted surface was covered by a film of partially cracked/polymerized hydrocarbons during the implantation
2) the energy of the implanted ions caused the formation of an oxide such as gallium arsenite or arsenate which is not wetted nor dissolved by gallium.

In light of the difficulties, the agreement to within a factor of two is considered satisfactory. We shall continue attempts to secure reliable primary oxygen standards.

Following the above procedure, a heavily Te-doped GaAs crystal was analyzed for oxygen. The oxygen concentration was found to be between 0.5 and 1×10^{18} atoms cm^{-3}, a figure grossly in excess of the conservatively estimated detection limit of our method of 5×10^{16} oxygen atoms cm^{-3}. Alternatively, the detection limit may be stated as a fraction of 0.2 - 1 mono layers on the surface. Differentation between surface and bulk oxygen can be made in principle by limiting dissolution to a shallow surface layer by using a Ga melt almost saturated with GaAs. Figure B shows the time dependence of $(P_{O_2}/P_{O_2R})^{1/2}$ before and after dipping selected samples of GaAs into Ga when the amounts of detected oxygen were at the detection limits.

The sample corresponding to curves A and A' were those for GaAs sample, WORM-1, prepared by Dr. Jerry Woodall of IBM. It was made by re-growth in a quartz boat under a Ga_2O pressure greater than or equal to the pressure of Ga_2O in equilibrium with Ga_2O_3 at 900°C[1]. This sample was previously known to have had an unusually low trap concentration[2] Curve B was obtained using the GaAs sample, WA-1000, an undoped GaAs crystal also grown in quartz without deliberate oxygen doping by W. Allred at USC. These samples were amongst the ones showing the lowest optical absorption in the 10.6μm region.

Several conclusions were drawn from the above results:

(1) Gross amounts of oxide, i.e. a few monolayers as a possible oxide residue on the surface of GaAs cleaned by acid etches and water rinses are removed by heating in H_2 containing $\sim$ 6 ppm of H_2O for about 30 minutes at 600°C. This heating schedule is that used to equilibrate the samples before partially dissolving them in Ga.

(2) Oxygen was not detected in a sample grown under circumstances in which a deliberate attempt was made to provide an oxygen overpressure.

This prompted a speculation that oxygen might be present in the WORM-1 and WA-1000 samples and that it compensated the Si in these. Under these circumstances the dissolution of Si with oxygen in gallium might lead to the

formation of SiO_2 and not influence the emf of the cell. The reaction of Si and O dissolved in Ga, based on the typical fugacities of oxygen used and the assumption of ideality for Si, should proceed to completion. As such, oxygen in excess of twice that of Si would only be detected. The completeness of the Si-O reaction also suggested that the method could be used to estimate silicon uncompensated by oxygen in GaAs.

To test the reaction of Si with oxygen in Ga, a sample of Si-doped GaAs was dissolved in Ga containing a known amount of oxygen as determined by the cell emf. Evidence for the reaction of Si with oxygen is shown in Fig. C.

The rapid decrease in E at t = 0, the conversion time, indicated a decrease of oxygen which is attributed to the reaction of Si and oxygen and transit effects associated with incomplete mixing. The approach to a more uniform melt is associated with a gradual rise followed by the long term drift. Extrapolation of the long term drift assuming the Si-O reaction product to be $SiO_2(s)$ leads to an estimate of the Si concentration as being $4 \times 10^{18} cm^{-3}$. This is probably in fair agreement with the total silicon concentration of the sample. Here again we are forced to draw only semi-quantitative conclusions because of uncertainties in the standards.

In light of the previous results it is not surprising that we were unable to detect the presence of a suspected oxide caused by heating GaAs in air to $\sim$ 350°C for 30 minutes, a procedure known to decrease the optical transmission at 10.6μm.

References

1. Dr. Jerry Woodall, private communication
2. Dr. Gordon Kino, private communication

Expitaxial Growth of Semi-Insulating GaAs from Ga Solutions

S. T. Hoelke, P.S. Vijaykumar and J. M. Whelan

A horizontal epitaxial slider unit that can utilize oxygen pumping in the course of epitaxial growth has been designed and built. This and another unit will be available shortly for the growth of thick films which can be doped with Cr, Fe or Ni to make them semiinsulating. The purpose of growing such films is to prepare the semi-insulating crystals in a manner most likely to insure selective doping and its effects upon optical absorption at 10.6μm.

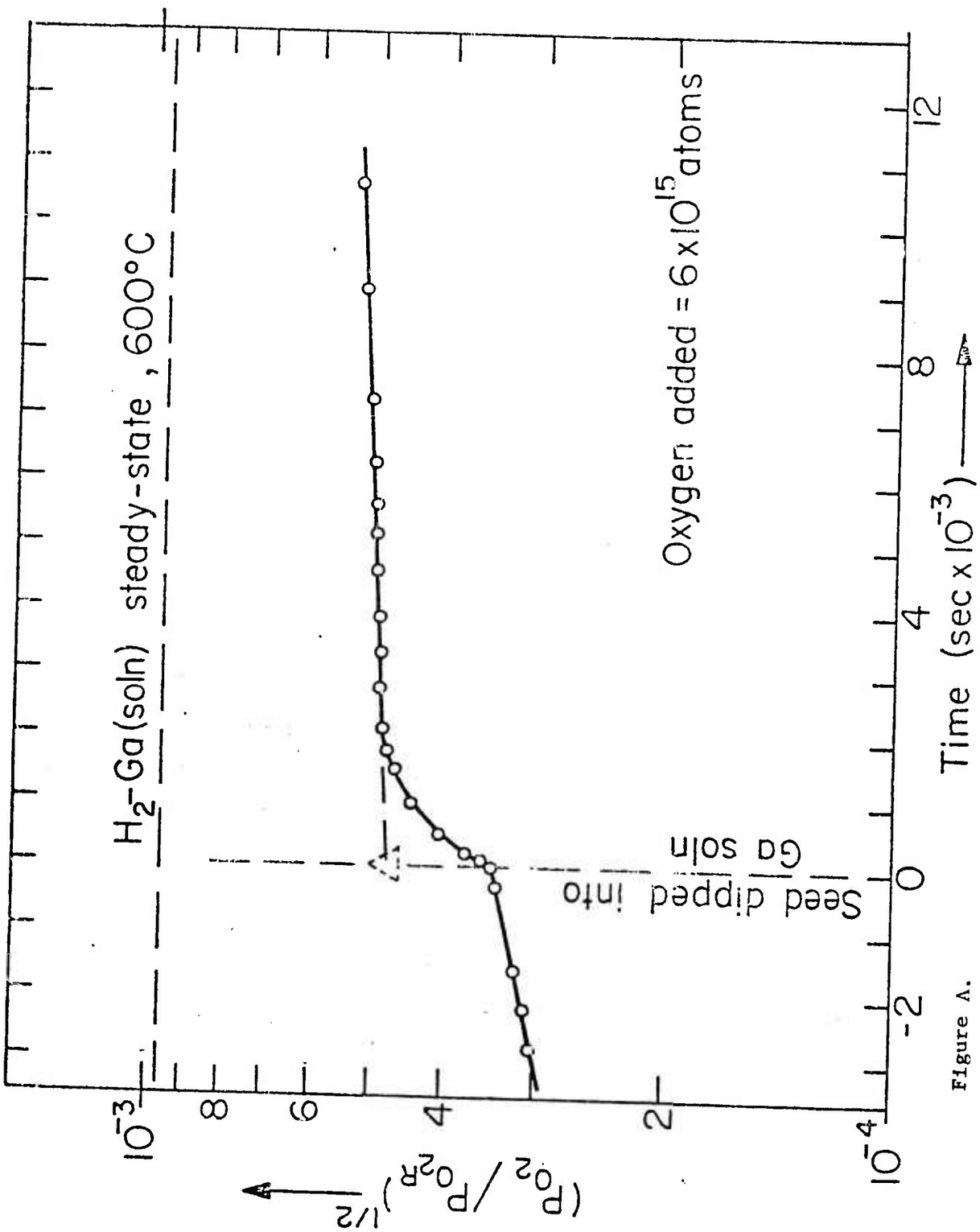
H_2-Ga(soln) steady-state , 600°C
Oxygen added = 6×10^{15} atoms
Seed dipped into Ga soln
$(P_{O_2} / P_{O_{2R}})^{1/2}$
Time (sec x 10^{-3})
10^{-3}
10^{-4}
8
6
4
2
-2
0
4
8
12

Figure A.

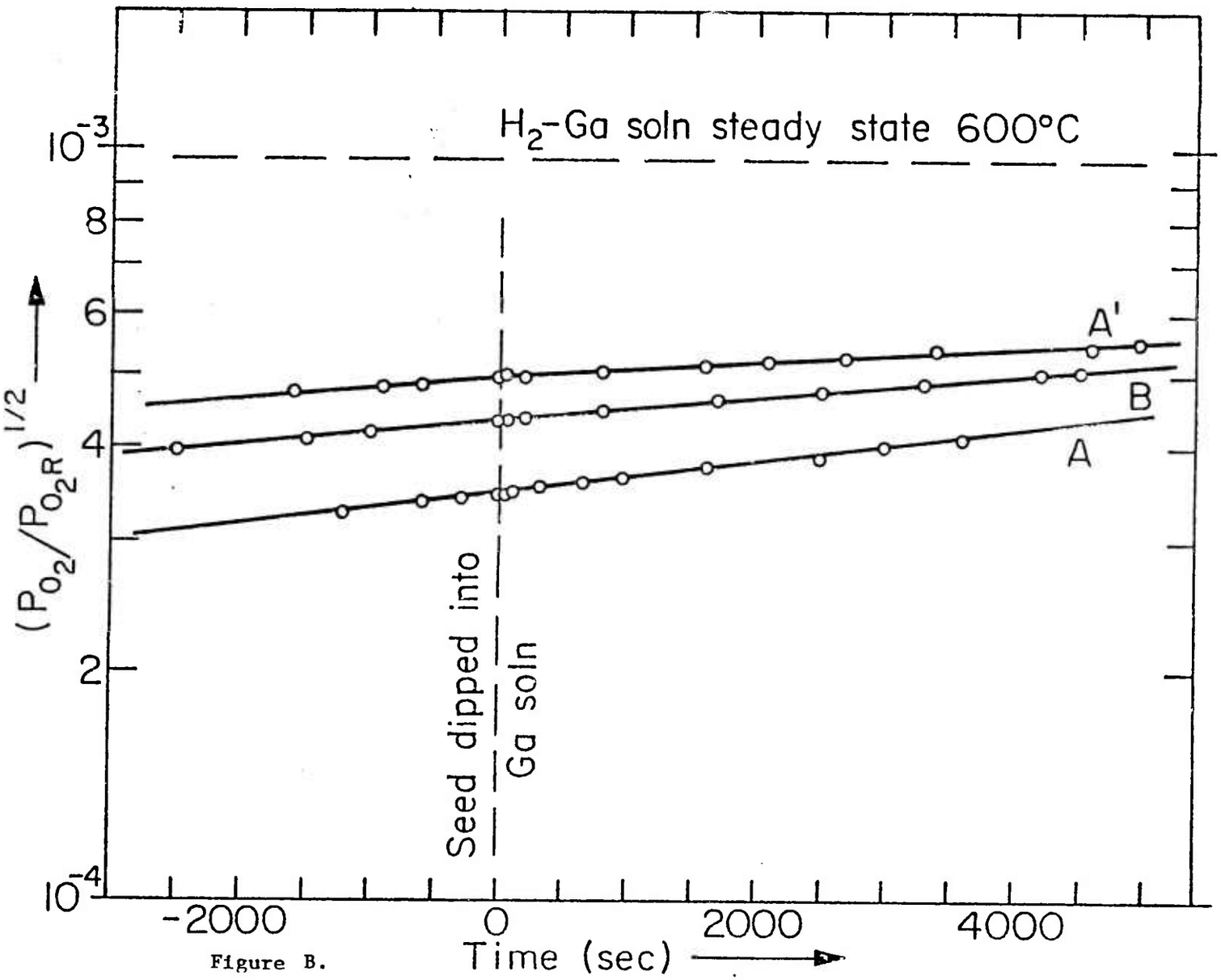
H_2-Ga soln steady state 600°C
10^{-3}
8
6
4
2
10^{-4}
$(P_{O_2}/P_{O_2R})^{1/2}$
A'
B
A
Seed dipped into Ga soln
-2000
0
2000
4000
Time (sec)

Figure B.

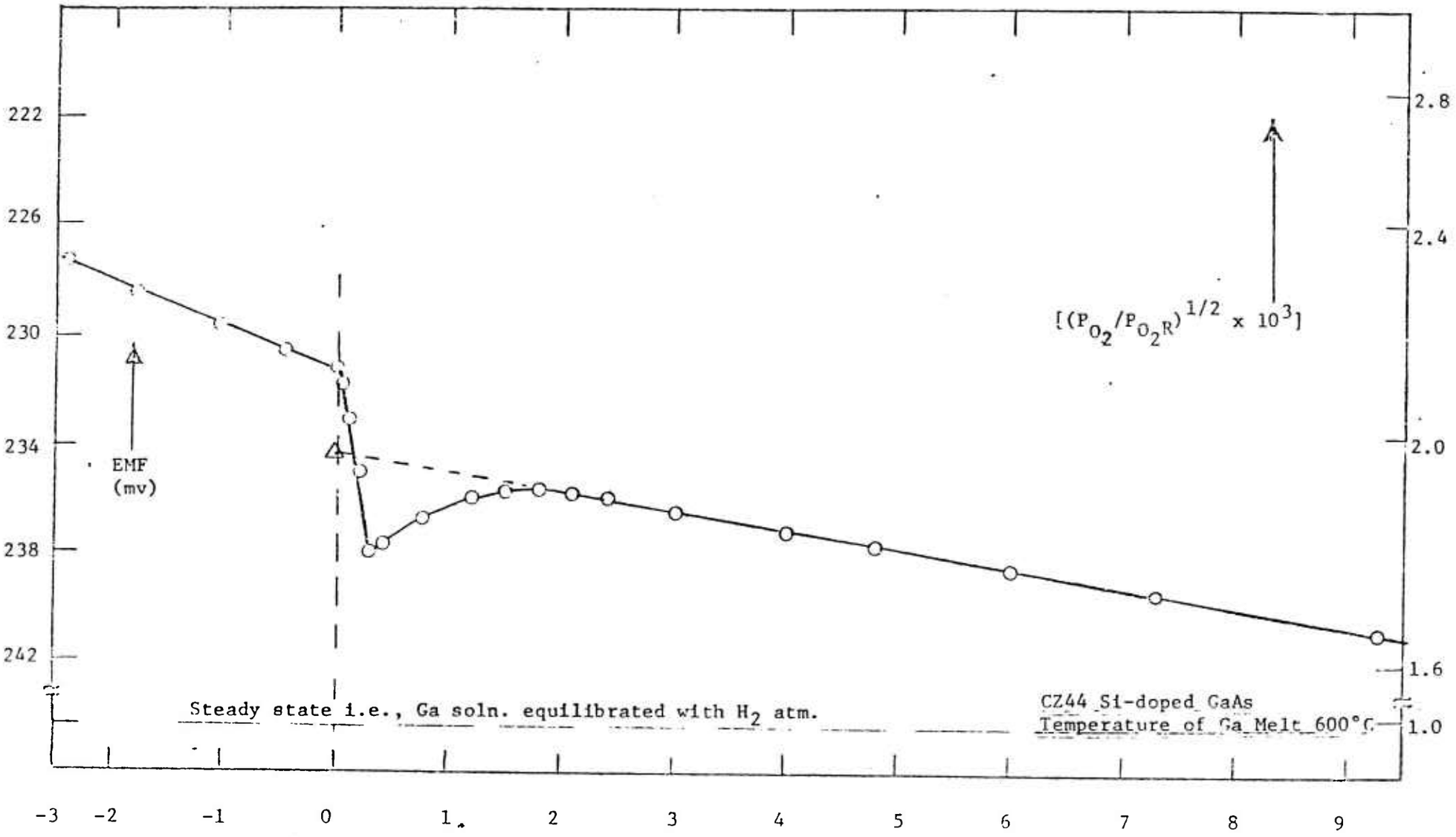
222
226
230
234
238
242
2.8
2.4
2.0
1.6
1.0
EMF
(mv)
$[(P_{O_2}/P_{O_2R})^{1/2} \times 10^3]$
Steady state i.e., Ga soln. equilibrated with H_2 atm.
CZ44 Si-doped GaAs
Temperature of Ga Melt 600°C
-3
-2
-1
0
1
2
3
4
5
6
7
8
9
TIME (sec x 10^{-3})

Figure C.

a.2 Optimization of Alkali Halide Window Materials

P. J. Sclichta, R. E. Chaney

a.3a Summary of Results and Plans: Calorimetric measurements of high-purity melt-grown KBr cyrstals indicate a 10.6 micron bulk absorption coefficient of $0.0011 cm^{-1}$, which is still much higher than theoretically predicted. In order to more surely eliminate contamination by bromate ions, attempts were made to grow crystals from molten KBr purified by reaction with ethyl bromide; however, pyrolysis of the ethyl bromide caused the melt to become contaminated with carbon particles. Future work will include the growth of bromate-doped KBr from melt and the growth of pure and bromate-doped KBr from solution.

a.3b Optical Absorption of KBr: As described in previous reports, the 10.6 micron bulk absorption coefficient of our KCl crystals, grown from purified melts, is comparable to the lowest values obtained elsewhere[1,2] and is well below the limit of reliability for our present calorimetric apparatus. Therefore, pending improvements in that apparatus (see section f.1) we are currently concentrating on measurements in pure and doped KBr.

As described in the last report, single crystals of KBr have been grown from salt which was purified by ion-exchange, fractional crystallization and gas treatment of the molten salt with HBr and Br_2. Specimens for calorimetry were cleaved from these crystals without subsequent polishing since during our previous studies of KCl, we found that cleaved samples can produce better surfaces than our present polishing technique.

Initial attempts to measure the absorption by a calorimetric method were not successful due to scattering of the laser radiation to the thermocouple. This scattering was caused by deterioration of the crystal surfaces during the time the samples were mounted in the calorimeter. The results of subsequent measurements, presented in Table 1 and Figure 1, indicate a bulk absorption (α) of $0.0011 cm^{-1}$ and an absorption per surface (σ) of $0.00051 cm^{-1}$. It should be noted that positioning the sample in the beam so as to eliminate scattering was very difficult and that the uncertainty of this set of measurements is higher than for previous samples.

For comparison, calorimetric measurements were also made on KCl and KBr cleaved samples purchased from Optivac. These are used as seeds for crystal growth, as specimens for surface preparation studies, and as standard specimens for comparison between our results and those of other laboratories.

The calorimetric results of Optivac crystals in the "as-received" condition (cleaved at the factory) are listed in Table 2. Figure 2 and 3 show the fit

of the data to the equation

$$\beta\ell = \alpha\ell + n\sigma \qquad (1)$$

where β is the absorption coefficient per centimeter, ℓ is path length, σ is the absorption per surface and n is the number of surfaces.

The results for as-received KCl, as shown in Figure 2, indicate an α of $0.00066 cm^{-1}$ and a σ of $0.0021 cm^{-1}$. Other samples, water lapped at the factory, had such cloudy surfaces that they were not measurable. The same was true of the water lapped KBr specimens.

For comparison, Table 3 lists our results for our own KCl crystals, as presented in the previous quarterly report.

The measurements on Optivac KBr cleaved samples in the as-received condition were too unreliable to permit extrapolation to estimate α and σ. This was because of excessive scattering of radiation (apparently from the surface) which made reliable measurements difficult to make. The minimum surface absorption, from Figure 3, is in the region of $0.002 cm^{-1}$. Evaluation of KCl and KBr samples with freshly cleaved surfaces are now in progress. Polishing techniques are being re-evaluated and a modification of Dyer's apparatus[3] may soon be constructed. Measurements on both cleaved and polished KBr crystals will be made during the next quarter.

a.3c Growth of KBr Crystals: It has been suggested[2] that much of the 10.6 micron absorption in impure KCl and KBr crystals might be due to the presence of chlorate ions in KCl and bromate ions in KBr. Although, it is difficult to understand how bromate ions could survive in molten KBr in a HBr atmosphere, it must also be conceded that bromate is a likely impurity in KBr and would not tend to be removed by ion exchange or fractional crystallization. Accordingly, since bromate is a strong oxidizing agent, it was decided that a more reducing reactive gas should be used in the final stages of purification. Of the gases described in Lebl and Trnka's original article on reactive atmosphere processing[5] ethyl bromide seemed most suitable. Preliminary experiments with this reagent, however, have been less than satisfactory because of its tendency to pyrolysis. During gas treatment of the molten salt, a heavy black deposit of carbon formed on the silica tube of the crystal puller and obscured visibility enough to seriously interfere with the seeding and growth process. Moreover, carbon deposits were also apparent on the inside of the bubbling tube, indicating that the decomposition of C_2H_5Br began before it bubbled through the melt. A few particles of carbon were found in the resolidified polycrystalline salt;

these were probably dislodged from the bubbling tube. There are no indications that carbon is formed in the molten salt. However, since cleaning the system between the gas treatment and crystal growth stages would allow possible contamination of the salt with atmospheric gases and residual water adhering to the fused silica liner, it seems inexpedient to continue using ethyl bromide. Future experiments will probably involve reagents such as CH_2Br_2 and CBr_4 sublimed into a carrier gas.

Work is also progressing on the growth of KBr crystals from melts doped with $KBrO_3$ and on the growth of KBr crystals from aqueous solution.

References

1. J. W. Davisson, M. Hass, P. H. Klein, and M. Krulfeld, Third Conference on High Power Infrared Laser Window Materials, November 12, 13, 14, 1973 - Agenda and Abstracts, p. 78

2. T. F. Deutsch, ibid, p. 80

3. L. D. Dyer, Rev. Sci. Instr., 34, (1963), pp. 1114 - 1116

4. M. Lebl and J. Trnka, Zeit. Phys., 186, (1965), pp. 128 - 136.

TABLE 1

Results of Absorption measurements of KBr at 10.6 microns

All samples were freshly cleaved

Crystal	Specimen	L(cm)	$\beta(cm^{-1})$	βL	Average βL
KBr 1 - 1	A	.7859	.00260	.00204*	.00199
			.00269	.00212	
			.00232	.00182	
	B	1.318	.00203	.00268	.00242
			.00210	.00277*	
			.00192	.00253	
			.00181	.00239	
			.00164	.00216	
	C	.4486	.00307	.00138	.00130
			.00298	.00134	
			.00294	.00132*	
			.00265	.00119	
			.00280	.00126	
			.00288	.00129	
	D	.2647	.00548	.00145	.00141
			.00513	.00136	

*Indicate sample repositioned between measurements.

TABLE 2

Results of Absorption measurements of Optivac KCl and KBr

All samples were cleaved at factory

Crystal	Specimen	L(cm)	$\beta(cm^{-1})$	βL	Average βL
OPT. KCl	1 ('a' axis)	5.393	.00194 .00226 .00211	.01048 .01217 .01140	.01135
	1 ('b' axis)	1.090	.00464 .00430 .00507	.00505 .00468 .00553	.00509
	2 ('a' axis)	2.040	.00432 .00453 .00339	.00881 .00931 .00692	.00835
	2 ('b' axis)	0.7117	.00802 .00737 .00655 .00890	.00571 .00525 .00466 .00634	.00549
OPT. KBr	1 ('a' axis)	5.235	.001207 .000989 .000991	.006319 .00518 .00519	.00556
	1 ('b' axis)	1.114	.00460 .00549 .00447	.00513 .00611 .00498	.00541
	2 ('a' axis)	2.033	.00258 .00258 .00247	.00525 .00525 .00502	.00517
	2 ('b' axis)	.7407	.00219 .00393 .00329	.00216 .00291 .00244	.00268

TABLE 3

Summary of Results of Absorption Measurements at 10.6 Microns on KCl Crystal 3-7

Sample	Surface Preparation	$\alpha(cm^{-1})$	σ
KCl 3-7 A, B and C	Polished	0.00025	.0007
KCl 3-7 D and E	Freshly cleaved	<0.0001	~0.0001

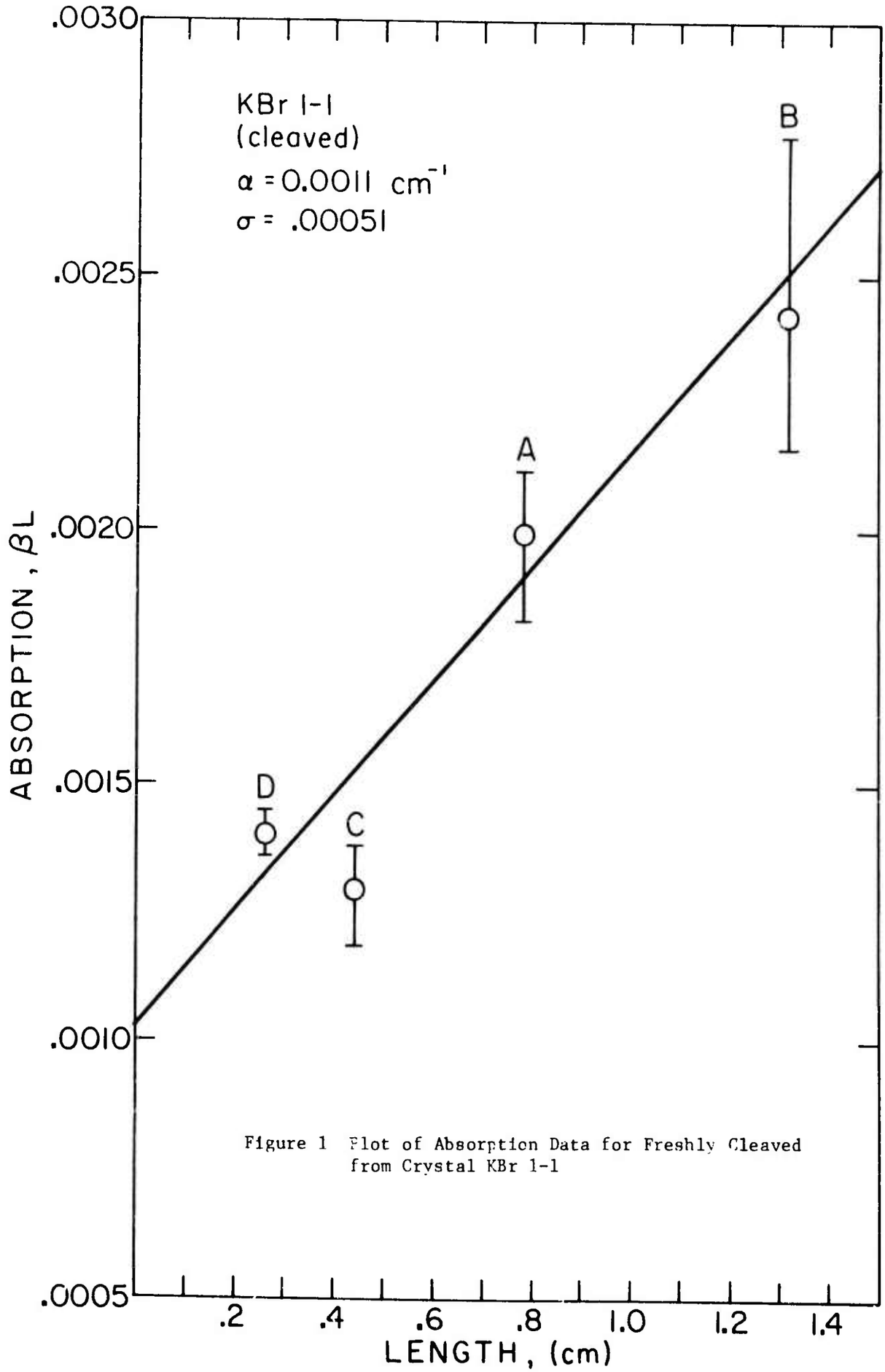

Figure 1 Plot of Absorption Data for Freshly Cleaved from Crystal KBr 1-1

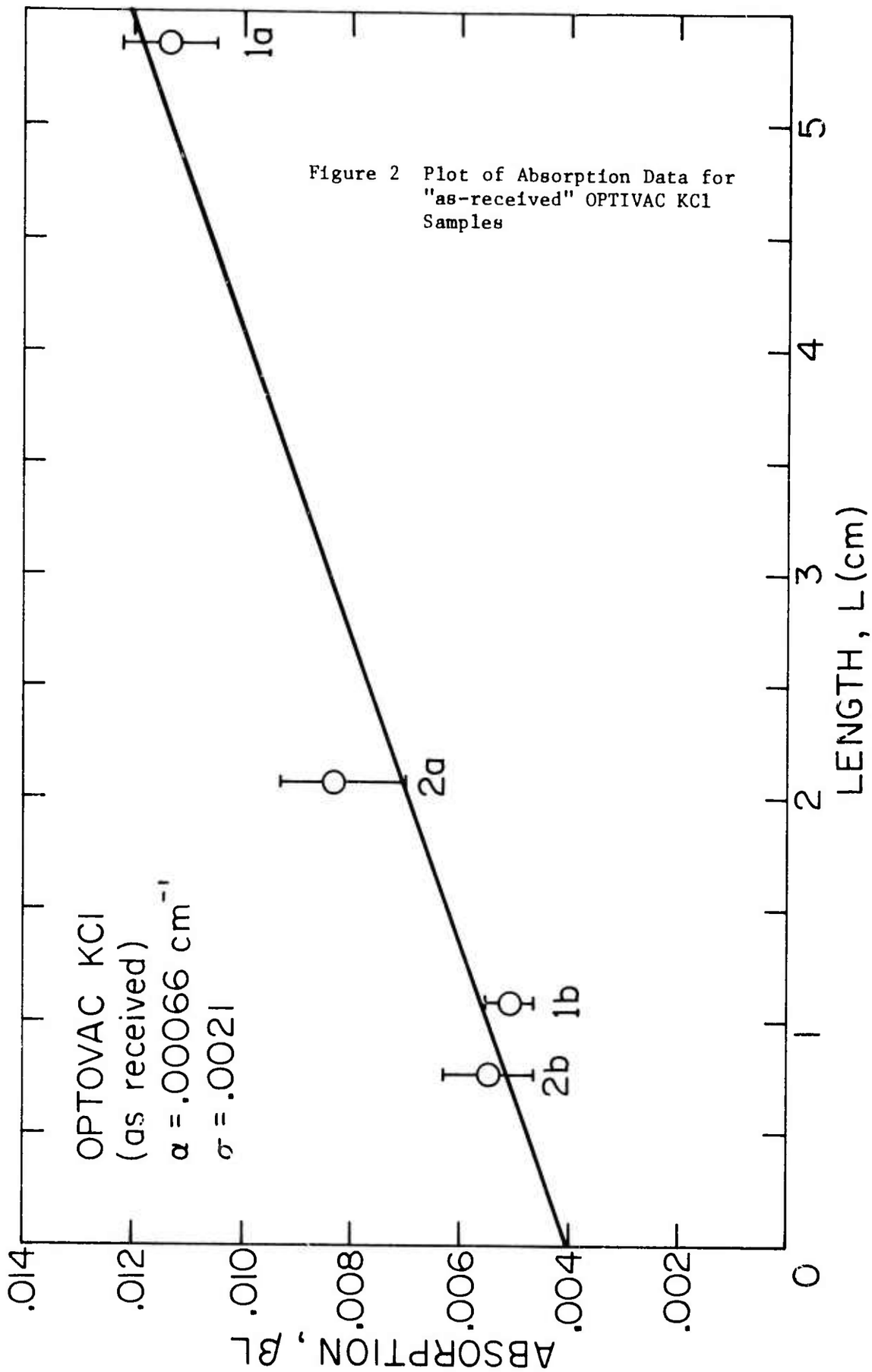

Figure 2 Plot of Absorption Data for "as-received" OPTIVAC KCl Samples

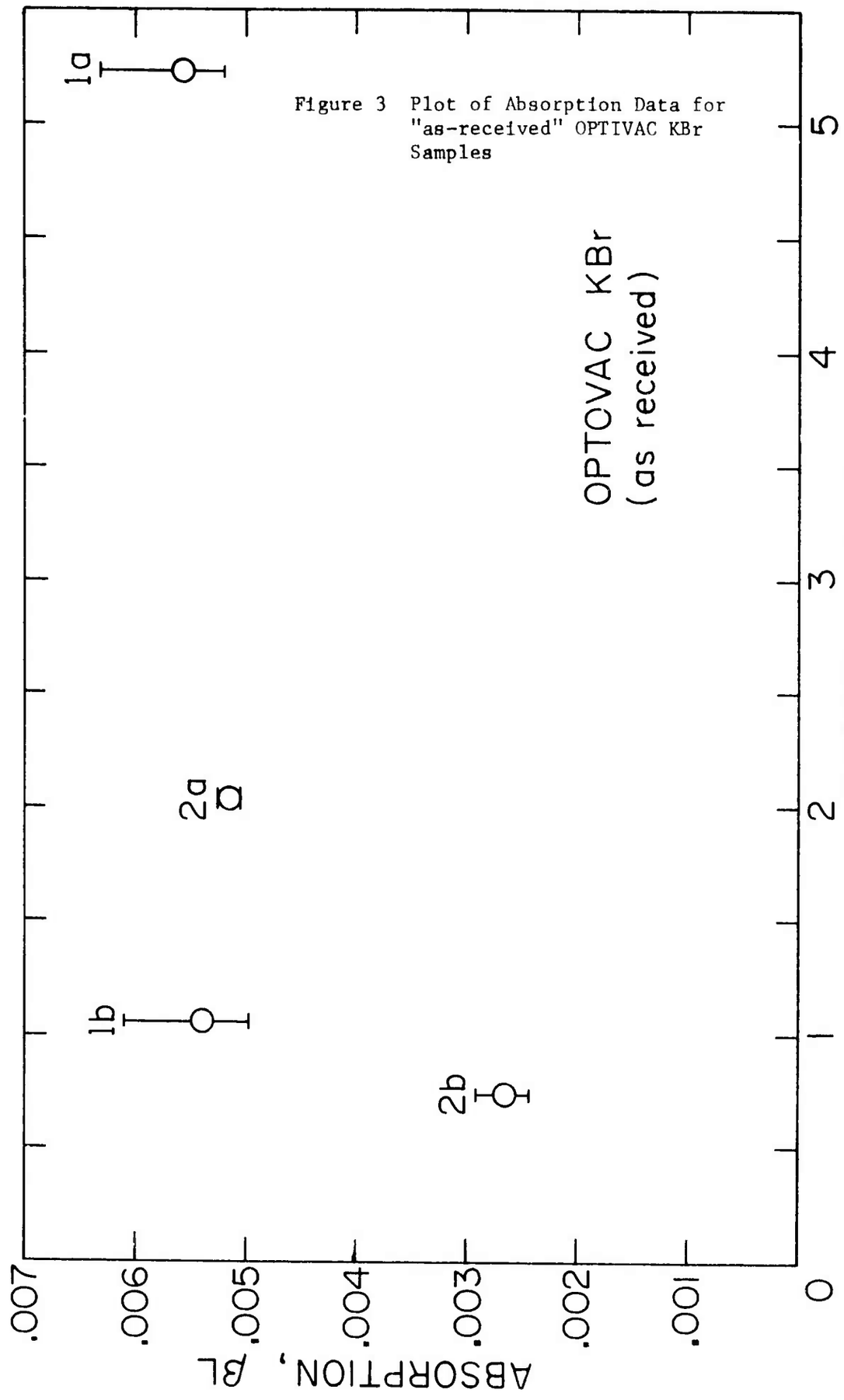

Figure 3 Plot of Absorption Data for "as-received" OPTIVAC KBr Samples

a.3 Chemical Vapor Deposition of Bulk GaAs Crystals

W. R. Wilcox, E. A. Miller

a.3a Introduction: We wish to summarize the effort of the past 18 months which was directed toward growth of bulk GaAs by the open tube CVD method, since the project has now ended. Particular emphasis will be on the last quarter's work, wherein we obtained smooth deposits 1 to 2 mm thick on GaAs substrates.

a.3b Experimental Procedure: An open tube epitaxial reactor was constructed, which used the $AsCl_3$-Ga-H_2 deposition system. This system is most often used in the semiconductor process industry for growth of high purity GaAs films by CVD methods. We established operating conditions favorable for the growth of thin films, but found that these conditions were not suitable for long term thick layer growth. Next, our effort consisted of experimentally determining the optimum conditions for substrate temperature, $AsCl_3$ mole fraction in the gas substrate orientation, and growth time.

a.3c Results and Discussion: Several long runs were completed which resulted in severe substrate etching. This was accompanied by dendritic overgrowths which apparently consumed reactants from the gas stream directly above the substrates. By reducing the $AsCl_3$ supersaturation (lower $AsCl_3$ mole fraction in the gas) we were able to minimize dendritic growth. It seems, however, that given enough time dendritic overgrowth occurs regardless and acts as a factor limiting deposit thickness. For example, a 9 day run (CVD #21) gave smooth deposits, while a 27 day run under the same conditions (CVD #22) resulted in severe etching and dendritic overgrowths (see Table I).

From results of previous runs, we selected operating conditions that yielded deposits 1 to 2 mm thick in 7 days. The substrate orientation was {100}, which reportedly has a slower growth rate than other orientations tested, but more uniform deposits usually occur. Figure 1 shows the results of this run (CVD #26); note the clusters of GaAs deposits on the substrate holder, and the blade-like dendritic growths on substrate #1 located at the tip of the holder. Also see Figure 2 for a close-up view of substrate #1. The blades on substrate #2 (2nd from the tip of holder) are shown in Figure 3.

Substrate #3 was further examined. Note the appearance of large individual grains, Figure 1, the boundaries of which were revealed by inclusions and voids after lapping and chemical polishing. The orientation of these grains remained in the {100} direction, however. All deposits in this run had many small voids and inclusions, possibly due to small air leaks in the system. See Figure 2 for example.

Table I summarizes some of the operating conditions and results obtained during this program.

a.3d Optical and Electrical Properties: Som IR absorption and Hall data were taken on the deposited films. From run CVD #21, we were able to obtain a sample 4 mils thick after lapping away the substrate. Results from this sample, see Table II, show that the material obtained is approximately of the same quality as typical melt grown GaAs. These rather poor results could have been caused by the small voids and inclusions observed in the sample. Perhaps if our system had been cleaner, much better results would have been obtained. Other determinations were made on samples with many small ($\simeq 0.5mm^2$) polycrystalline inclusions in them; results in these cases were even worse. An absorption measurement at 10.6μ was made on one of the blades grown in run CVD #26. The absorbance was so high that a hole was burned through the sample at 5 watts incident power. In addition, operation at the lower $AsCl_3$ mole fractions (necessary to produce thick films) increases the tendency for impurity incorporation (mainly Si)[1], thus further degrading the electrical properties.

References

1. J. V. DiLorenzo, J. Crystal Growth 17, 189 (1972)

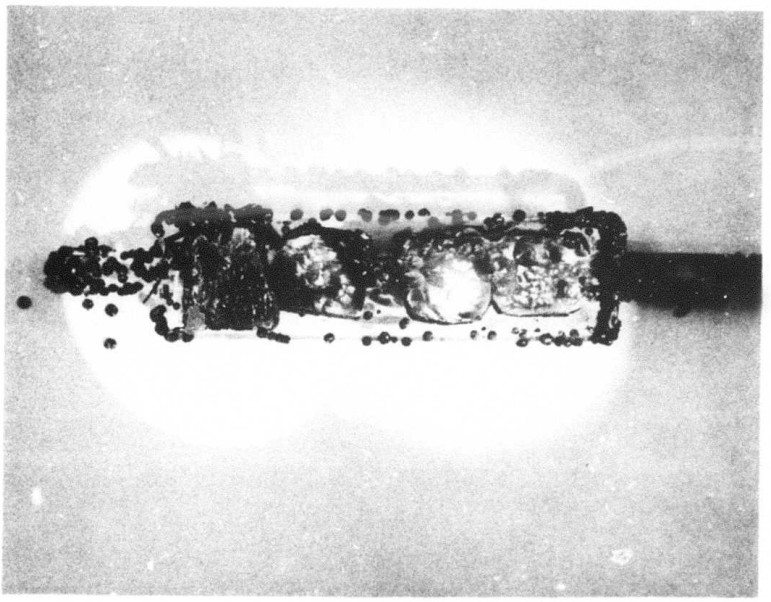

Figure 1 CVD #26 0.7X

Figure 2 CVD #26 Substrate #1 4X

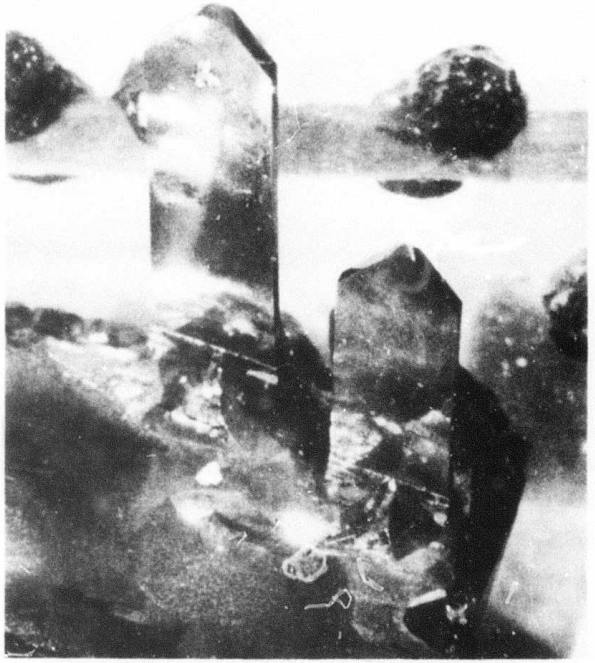

Figure 3 CVD #26, Stustrate #2 10X

TABLE I

SUMMARY OF RUNS 3/1/73 - 11/30/73

Run #	$AsCl_3$ Mole Fraction	Length of Run	Substrate Orientation	Substrate Temp.	Results
CVD #13	6×10^{-3}	1 Day	{100}	750°C*	Growth with many hillocks
CVD #16	5.6×10^{-3}	1 Day	{111} A & B {100}	770°C	Smooth growth on {100}, uniformly rough deposit on {111} A
CVD #17	5.6×10^{-3}	5 Days	{111}A	750°C	Severe dendritic growth, slight substrate etching
CVD #19	2.8×10^{-3}	3 Days	{111}A 4 pcs	735 - 765°C	Deposit uniform, but rough, few dendrites
CVD #21	2.3×10^{-3}	9 Days	{111}A 2 pcs {100}2 pcs	735 - 765°C	Growth pits {111}A; specular, hillock growth {100}
CVD #22	2.2×10^{-3}	27 Days	{111}A 2 pcs {100} 2 pcs	735 - 765°C	Severe etching on all substrates
CVD #24	5.6×10^{-3}	5 Days	{111}A 2 pcs {110} 2 pcs	775 - 795°C	Rough polycrystalline deposits, some specular areas
CVD #25	3.5×10^{-3}	7 Days	{111}A 2 pcs {110} 2 pcs	765 - 785°C	Rough polycrystalline deposit {110}, specular polycrystalline depost {111}A
CVD #26	4.5×10^{-3}	7 Days	{100} 4 pcs	745 - 775°C	Smooth, specular, 1 - 2 mm thick deposits, many small voids, blades grew in high temperature regions

*Temperature profile as reported by C.M. Wolfe, A. G. Foyt, Electrochem Tech., 6, 208 (1968)

TABLE II

SUMMARY OF ELECTRICAL AND OPTICAL MEASUREMENTS

Run #	Orientation	Thickness	Resistivity	Hall Mobility	Carrier Concentration	Absorption Coefficient (10.6μ)
CVD #21 Wafer #2	{100}	5 mils	0.16Ω-cm	$3400 \frac{cm^2}{v \cdot sec}$	5×10^{15} cc^{-1}	
CVD #21 Wafer #4	{100}	4 mils				$0.046 cm^{-1}$
CVD #24 Wafer #2	{111}A Polycrystalline inclusions	5 mils	0.35Ω-cm	$280 \frac{cm^2}{v \cdot sec}$	7×10^{16} cc^{-1}	$2.1 cm^{-1}$
CVD #26 Wafer #3	{100}	0.7mm	0.06Ω-cm	$980 \frac{cm^2}{v \cdot sec}$	1×10^{17} cc^{-1}	$0.9 cm^{-1}$

b.1 Fabrication of Polycrystalline IR Window Material

S. M. Copley, J. M. Whelan and V. Rana

The aim of this part of the program is to produce samples of laser window materials in polycrystalline form by a novel hot pressing technique involving the use of volatile sintering aids. This technique has been described in detail in previous quarterly reports.

Experiments have been carried out by hot pressing CdTe powder with liquid Cd as a sintering aid. CdTe powder, 99.999 pct. pure, was obtained from Research Organic/Inorganics. This powder is produced by coprecipitating Cd and Te from solution. This coprecipitation is carried out by reducing acidic solutions of Cd and Te with hydrazine monohydrochloride (H_2H_4HCl). The resulting precipitate is washed many times with hot water. The water is subsequently driven off by heating to 130°C for 2 or 3 days in vacuum. Average grain size of the powder used in our experiments is 1μm. Extra Cd, to be used as a sintering aid, added to the charge, is either in powder form (99.999 pct pure, -100 mesh) or as shots (99.999 pct pure); both obtained from Cominco American Incorporated.

It has been possible to prevent any loss of Cd from the charge by using the die configuration shown in Fig. 1. By utilizing the chill, Cd in the top recess of the die is kept at a slightly higher temperature ($\Delta T \cong 20°C$) than the Cd in the charge so that it provides the overpressure of Cd required. The Cd at the top is prevented from escaping by covering it with LiCl-KCl eutectic (melting point 355°).

To form the compact, the die is placed in the furnace inside the hot pressing chamber and the chamber is evacuated to a pressure of 30 micron of Hg or better. The powder is then hot pressed; two procedures of hot pressing have been employed. In the first procedure, pressure is applied to the die plunger at room temperature and is maintained while the temperature is raised at a rate of approximately 2°C/min. to the final desired temperature. Curve (a), Fig. 2, shows a typical curve for densification obtained by this procedure. Microscopic examination of such compacts showed that Cd was not able to disperse throughout the compact uniformly, but was segregated at several places. In the second procedure, the charge was first heated up to the desired temperature, and then pressure was applied. All the compacts obtained in this manner were superior to those obtained following the first procedure, curve (b) Fig. 2. The Cd was much better dispersed, and after wetting the grains during compaction, the extra Cd was squeezed out between the plunger and the die wall. There were still, however, certain areas of compact where densification was poor. Fig. 3 shows a well compacted area, while Fig. 4 shows a poorly compacted area in the same compact.

Severe sticking of CdTe compact to the die made from Speer graphite grade 580, was observed. There was also evidence of Cd effusing through the walls of the die. Using Poco graphite grade HPD-1, these problems of Cd effusion and sticking have been almost eliminated.

CdTe powder used in our experiments has been found to contain some volatile matter. Severe outgassing from the charge was noted in all the runs (Fig. 5). This volatile matter could be any of the reagents used in synthesis and not completely washed away (e.g. hydrazine monohydrochloride) or any of the intermediate compounds not completely converted to the final product CdTe (e.g. $Cd(NH_2)_2$ or $CdTe\ N_2H_4$). Such volatile matter if not removed prior to compaction gives rise to gases that can get trapped inside the compact. It may be responsible for the voids seen in the poorly compacted samples. It may also prevent the liquid Cd from completely wetting all the particles. It is also, of course, necessary to remove this volatile matter in order to obtain a high purity compact.

Efforts are underway to characterize and eliminate the volatile impurities. Initially, the powder will be heated to a temperature higher than the boiling point of all suspected impurities and its effects on densification seen. Powder refinements under H_2 gas flow will also be tried.

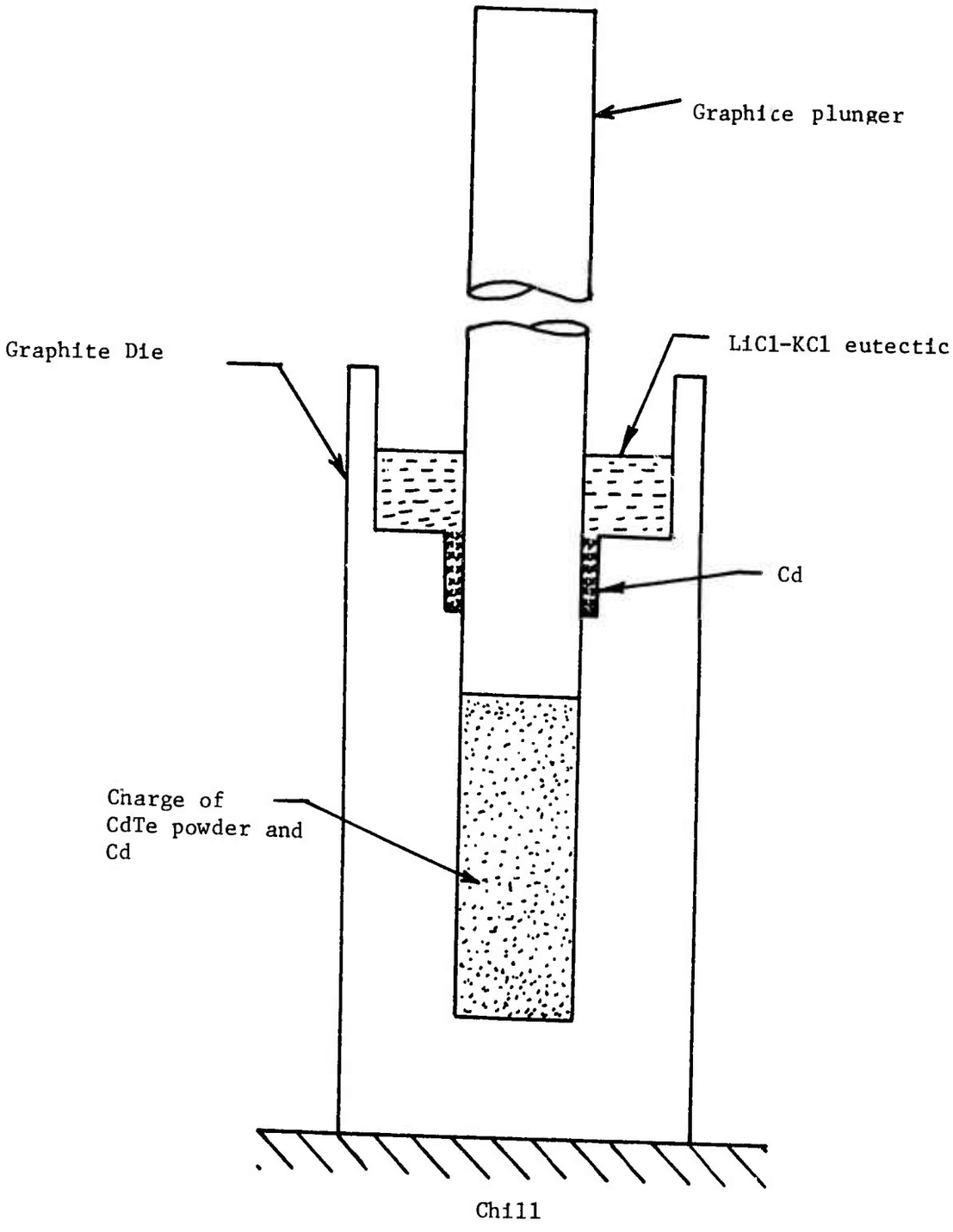

Fig. 1: Die configuration before hot pressing

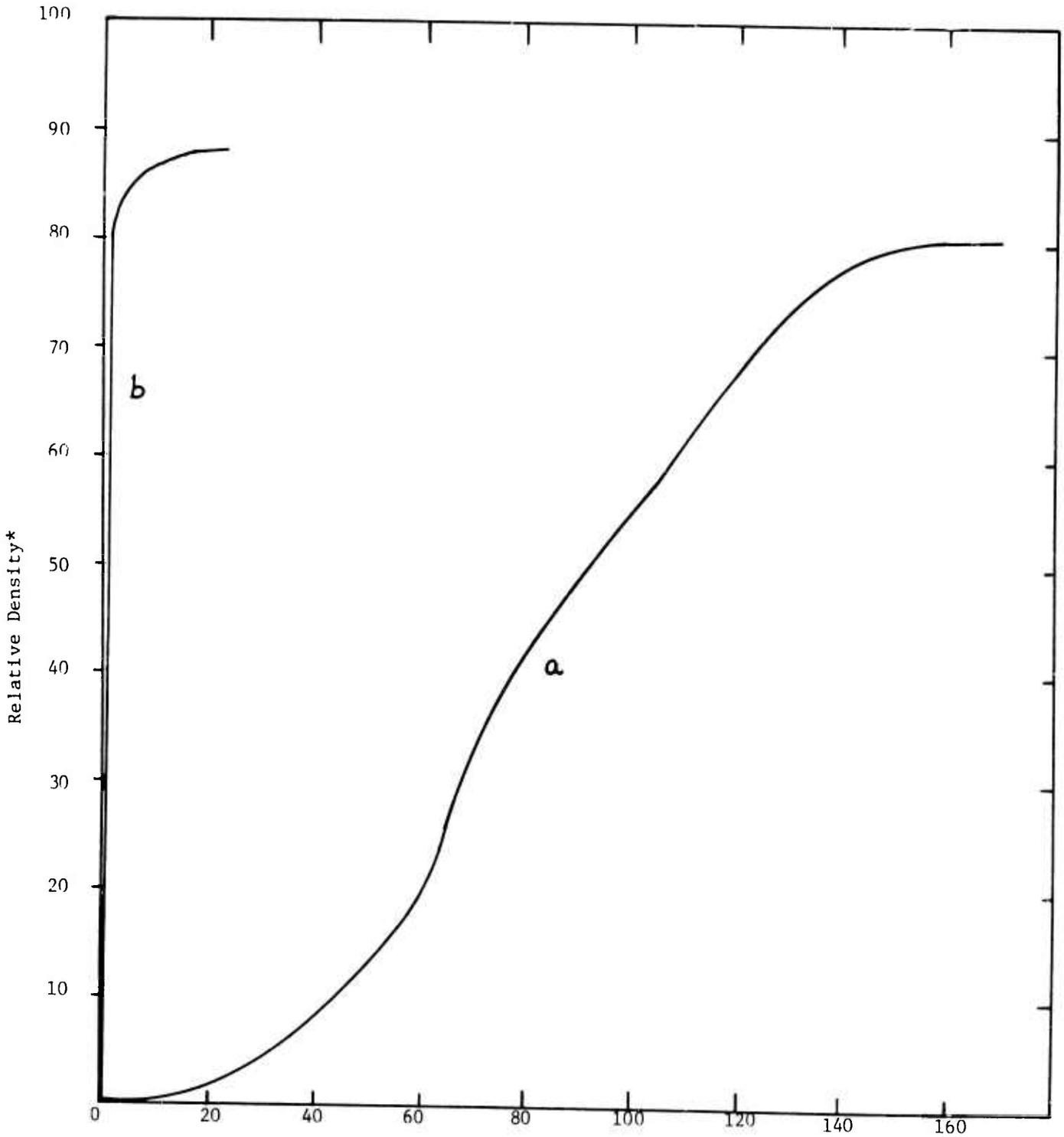

Fig. 2 (a) 1000 psi applied at room temperature and maintained, while temperature is raised at the rate of 2°C/min to 400°C
(b) charge is heated to 400°C and kept at that temperature while 3000 psi is applied for 15 minutes.

*Based on the theoretical density of CdTe of 5.86 gms/cm^3

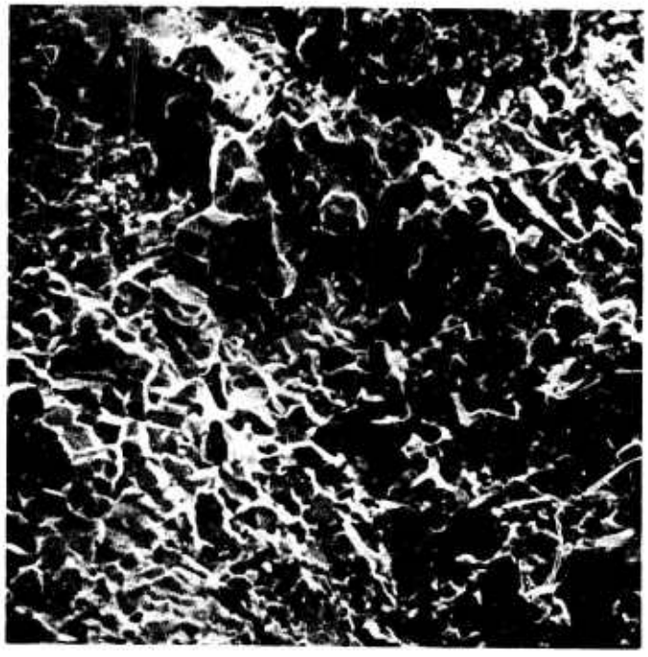

Fig. 3 Fracture surface of a compact pressed at 3000 psi after heating to 400°C

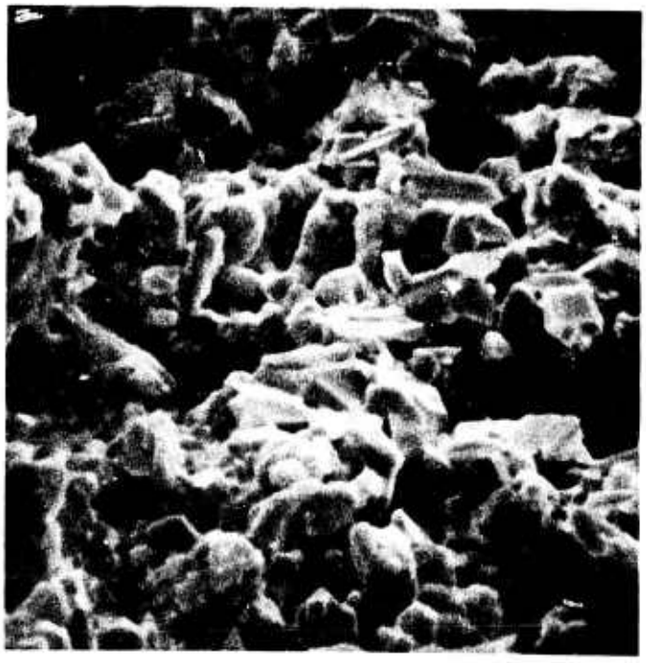

Fig. 4 Fracture surface of a compact pressed at 3000 psi after heating to 350°C

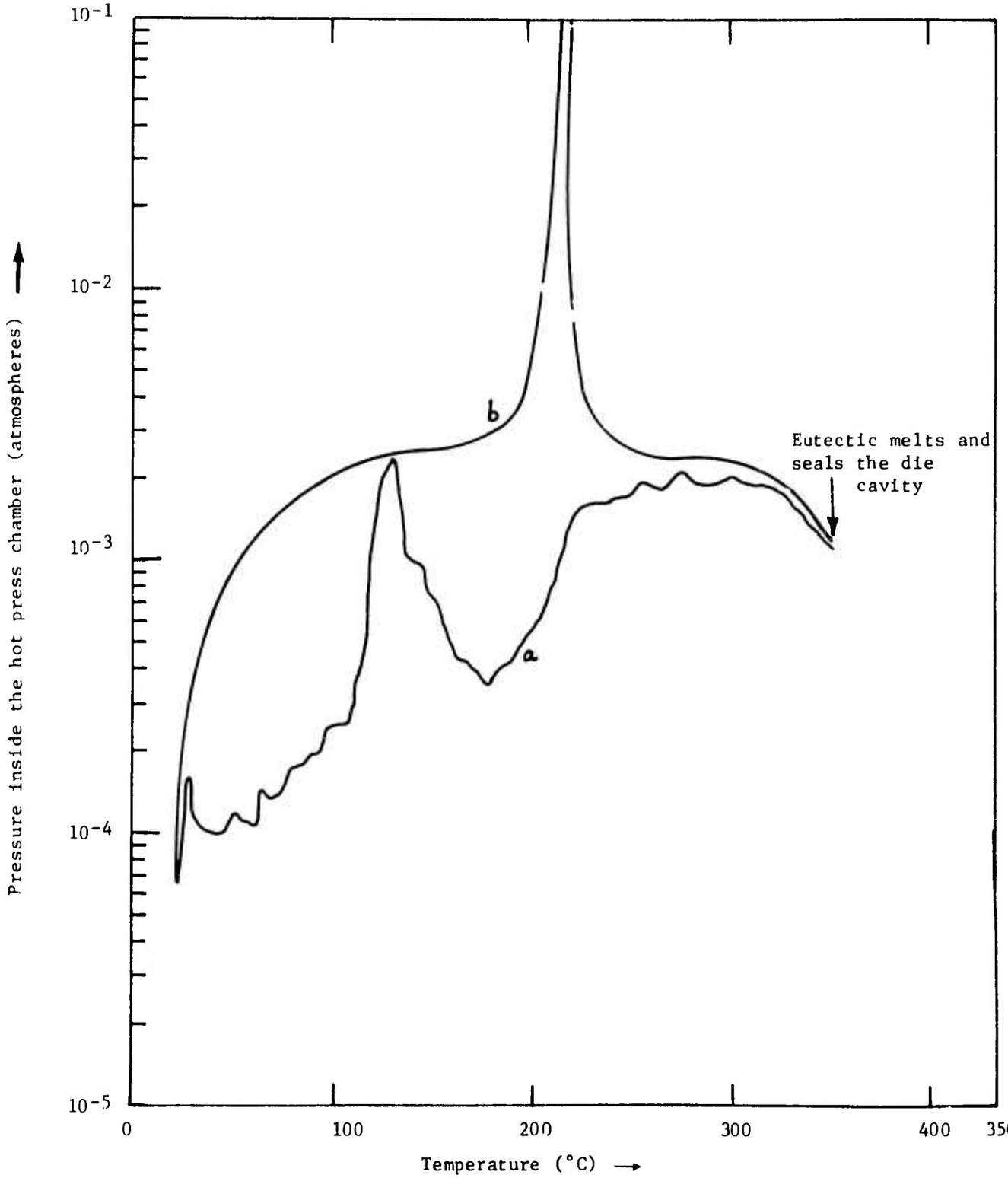

Fig. 5 Outgassing from the powder on heating in vacuum
(a) When temperature is increased at the rate of 2°C/min.
(b) When set point is set at 400°C (time to reach 400°C = 60 min.)

c.1 Mechanical Behavior of III-V and II-VI Compounds

S. M. Copley and V. Swaminathan

The objective of this investigation is to characterize the mechanical behavior of various candidate window materials under different conditions and to identify the important mechanisms of plastic deformation and fracture. In this report we will summarize briefly the results to date and indicate the experiments that are in progress.

c.1a Results to Date:

c.1a.1 Micro Structural Characterization: We have employed T.E.M. to characterize the microstructure of several types of GaAs which were used in the investigation of mechanical properties and also several types of high resistivity GaAs with low absoprtion coefficients investigated by Steier and co-workers as part of this program. The results of this investigation were reported in Quarterly Technical Report #4.

c.1a.2 Anomalous Diffraction Effects:* Diffuse intensity streaks and extra spots have been observed in transmission electron diffraction patterns of gallium arsenide single crystals. The configuration of these diffuse streaks and extra spots and their intensity have been studied as a function of crystal orientation and temperature. The geometry of the diffuse streaks and extra spots can be interpreted, respectively, in terms of the intersections of {110} sheets and <111> spikes of diffuse intensity in reciprocal space with Ewald's sphere. The presence of {110} sheets of diffuse intensity is explained on the basis of thermal diffuse scattering of electrons by low frequency acoustic phonons with wave vectors lying on {110} planes. The presence of <111> intensity spikes is also attributed to thermal diffuse scattering and is explained as a combined effect of lattice symmetry and phonon anisotropy. This work was presented at the Third Conference on High Power Infrared Laser Window Materials, and will be published in the conference proceedings.

c.1a.3 Stress-Strain Behavior: Stress-strain curves have been obtained for Si-doped GaAs single crystals to <100> and <111> at temperatures ranging from 250 to 550°C. In both orientations, slip is shown to occur only on {111} $\langle 1\bar{1}0 \rangle$. Repeated yielding experiments on GaAs crystals, both undoped and doped with Si, Cr and Zn indicate that Si-doped crystals (n-type) have a greater yield

*Work described in this section was carried out in collaboration with Professor G. H. Narayanan, Dept. of Materials Science, U.S.C.

stress than undoped crystals, and undoped crystals have a greater yield stress than Zn-doped crystals (p-type); Cr-doping does not significantly affect the yield stress. The effect of impurities is attributed to dynamic hardening through the formation of tetragonal defects involving vacancy-solute pairs. Extensive crack formation due to deformation is not observed. Compression specimens normally failed by breaking into several columnar fragments parallel to the stress axis. The results of this work were presented at the Third High Power Infrared Laser Window Materials Conference and will be published in the Conference proceedings.

c.1b Work in Progress:

c.1b.1 Impurity Hardening: Both theoretical and experimental work is currently in progress with the goal of relating the observed impurity hardening to the presence of tetragonal vacancy-solute pairs. GaAs single crystals doped with Si in the range of 10^{18} - $10^{19}/cm^3$ will be given different annealing treatments prior to deformation. These annealing experiments will be based on results by Kung and Spitzer[1]. Samples will be annealed at 1100°C for 15 minutes and they will be aged at 700°C, 600°C, and 450°C for specified periods of time. The effect of different concentrations of such solute-vacancy pairs on mechanical behavior will be studied. These experiments will be repeated with Te doped GaAs. Additional experiments on Si-doped with P and B are also being carried out to determine whether the solute-vacancy pair mechanism can explain the impurity effect in the elemental semiconductors.

Annealing experiments will also be carried out on GaAs containing Si > $10^{19}/cm^3$. Recent work at U.S.C. by Narayanan and Kachare has shown that annealing treatments on such highly doped crystals can cause the formation of a high density of prismatic dislocation loops of the vacancy type[2]. The annealing specimens will be tested in compression so that the effect of such prismatic dislocation loops on strength can be determined.

A special loading ram is being designed to carry out compression experiments at room temperature with precision alignment. The possibility of twinning as a low temperature deformation mechanism is being investigated.

c.1b.2 Cold Work and Process Annealing: We have established conditions for producing a recrystallized substructure in GaAs single crystals (see Quarterly Technical Report #4). It is believed that recrystallized material may well show improvements in absorption in comparison to melt grown single crystals. This is because the recrystallization process may lead to a redistribution of impurities along grain boundaries. Recrystallization experiments will be carried out on high resistivity Cr-doped GaAs obtained

from Bell and Howell. Specimens will be deformed to 20% at 550°C and then they will be annealed at 110°C for 10 minutes. This treatment will produce the recrystallized structure. Absorption as a function of wavelength will be measured before and after recrystallization.

c.1b.3 Mechanical Behavior of CdTe: During the renewal period of this project a basic investigation of the mechanical behavior of CdTe will be carried out. The material will be obtained from II-VI, Inc. Our main approach will be to emphasize the effect of thermal and thermo mechanical treatments on the defect structure and absorption of CdTe. The structure of specimens annealed under specified partial pressures of Cd and Te will be studied in collaboration with Dr. Kroger. The investigation of the differenct microstructures will be carried out by transmission electron microscopy. Thin foils of CdTe have already been successfully prepared. The orientation and temperature dependence of plastic deformation will be studied. Mechanisms of deformation, especially twinning, will be investigated.

References

1. J. Kung and W. Spitzer, unpublished research, University of Southern California
2. G. H. Narayanan and A. H. Kachari, unpublsihed research, University of Southern California

d.1 Dielectric Constant Measurements

Clarence R. Crowell, S. Joshi

Effort during this quarter was directed towards preparing more GaAs samples and confirming the dielectric constant measurements performed on the first sample and reported in September, 1973.

A second sample was prepared on another wafer of the same material. More precise marking for defining the active area was adopted. The sample was prepared by the same method as reported previously. Capacitance vs. voltage characteristics and capacitance vs. frequency characteristics were measured and were found to be the same as for the first sample. The variation of capacitance vs. frequency at liquid nitrogen temperature reported earlier was eliminated by better probe contacting technique and a flat capacitance vs. frequency curve was obtained at that temperature.

The measurements of thickness and area on the sample gave an effective dielectric constant about 10% higher than reported earlier. The thickness of the first sample was remeasured using present techniques and was found to be in agreement with a revised dielectric constant of approximately 13.6.

A need was felt to confirm this result on more samples and in particular to check the uniformity of a given sample. Accordingly, a sample was prepared from WA-100 GaAs material and gold electrodes were deposited to define dielectric capacitors. Area and thickness measurements on these capacitors gave an effective dielectric constant which varies about 3% from capacitor to capacitor.

From these results it is felt that the sample flatness and thickness measuring techniques still need to be improved to obtain the dielectric constant with better accuracy.

Preparation of dielectric capacitors on CdTe material for measuring the dielectric constant is also underway.

d.2 Study of Defects in II-VI Compounds

F. A. Kroger, F. Selim, B. V. Dutt

High temperature Hall effect measurements on lightly doped CdTe are being repeated to check on a small discrepancy between our data and those of Smith. The results will be compared with those of similar measurements in cooled crystals in order to see what happens to the native donors upon cooling.

We intend to grow variously doped crystals for local mode studies by Dr. Spitzer and resistivity Hall effect and 10μ absorption for ourselves.

A model to explain the properties of Ag-doped CdS has been developed, and the observed Hall and resistivity data are being interpreted on the basis of this model.

d.3 Damage Studies

L. DeShazer and M. Bass

During this quarter we began to assemble the pulsed CO_2 TEA laser for use in the 10.6μm high peak damage studies. A few of the pieces have been fabricated and a few components ordered. Most of the fabrication, assembly and testing will be completed during the next quarter.

e.1 Theoretical Studies of Absorption Mechanisms in IR Window Materials

R. W. Hellwarth and M. Mangir

e.1.a Determination of the Mechanism of Multi-Phonon Absorption in Pure Crystals

This quarter was devoted mainly to the search for a method by which one can determine unambiguously from experiment the relative contribution of multi phonon absorption in a given material of the two possible mechanisms: a) anharmonic interionic forces and b) the nonlinear dependence of the electric dipole moment on ionic displacements, i.e., the "nonlinear moment". We believe we have discovered the first practical method to achieve this. It is described in detail in Appendix I which is to appear in the Proceedings of the Third Conference on High Power Laser Window Materials (Air Force Cambridge Research Labs, 1973) ed. by Carl Pitha. As is pointed out there, so far the necessary data for our method exists only for LiF (from which we concluded that mechanism (a) dominates in pure LiF at room temperature). We are currently trying to collaborate with experimenters at USC and elsewhere in making the measurements necessary to determine the multi-phonon absorption mechanisms in III-V and II-VI window materials. For these materials the mechanism is especially unclear at this point.

A METHOD FOR MEASURING THE CONTRIBUTION OF THE NONLINEAR DIPOLE MOMENT TO MULTI-PHONON ABSORPTION*

ROBERT HELLWARTH and METIN MANGIR
Electrical Engineering and Physics
University of Southern Calif.
Los Angeles, Calif. 90007

Abstract

A method is proposed by which one may determine the separate contributions of the anharmonic interionic forces and of the nonlinear dipole moment of any material to the integral over IR frequencies of the imaginary part of its dielectric function (times the frequency). With this we show from existing data that the contribution of multi-phonon absorption to this integral for LiF is predominantly from anharmonic forces.

1. INTRODUCTION

In order to calculate the multi-phonon absorption in a given material, one must first know the relative contribution of the two possible mechanisms: A) anharmonic interionic forces, and B) the nonlinear dependence of the electric dipole moment on ionic displacements (or the "nonlinear moment"). For alkali-halides, it has been found consistent in, albeit approximate, calculations to neglect mechanism (B).[1] However, for some promising high power laser window materials, such as ZnSe, CdTe, and GaAs, the relative importance of the two mechanisms remains uncertain.[2]

We propose here an experimental method for assessing these mechanisms in any material. The method is based on the well known fact that the frequency shift(s) and width(s) of the fundamental infrared lattice absorption resonance(s) are insensitive to the nonlinear moment, whereas, multi-phonon difference- and summation-absorption bands are sensitive to both mechanisms.[1] At the present the only material for which enough data exists to apply the method is LiF, and we find that the anharmonic force mechanism (A) is indeed mainly responsible for the more prominant multi-phonon features in the absorption spectrum of LiF. (See Section 4).

Our method requires the measurement of the imaginary part $\varepsilon_2(\omega)$ of the dielectric constant, throughout the infrared, and at two or more temperatures. From this measurement one obtains an experimental determination of the integral in the following exact sum rule, in esu (proved in Appendix A)

$$\int_0^\infty d\omega\omega\varepsilon_2(\omega) = \frac{2\pi^2}{V} \Sigma_{\alpha,i} <(\partial M_x/\partial r_{i\alpha})^2>/m_\alpha \text{ sec}^{-2} , \qquad (1)$$

in which M_x is the operator representing the electric dipole moment along the principle dielectric x-axis for which ε_2 was measured. For optically isotropic materials this x-axis can be any axis and all principle dielectric constants are equal. The $r_{i\alpha}$ are the spatial coordinates (i=x,y,z) of all the N ions (α=1, 2,...N), with masses m_α, inside a macroscopic volume V of the crystal. The brackets <> indicate the quantum average.

The usefulness of (1) lies in the fact that the contribution of the averaged expression of the linear term in the dipole moment can be easily calculated exactly for many important types of crystals. To see this, we first write each ion coordinate as

$$r_{i\alpha} \equiv R_{i\alpha} + x_{i\alpha} , \qquad (2)$$

the sum of its average value $R_{i\alpha} \equiv \langle r_{i\alpha} \rangle$ (for some temperature) and its deviation $x_{i\alpha}$ from this average value. Then the dipole moment in a volume V of the crystal at this temperature can be expanded in a Taylor series in the $x_{i\alpha}$:

$$M_x = \Sigma_{i\alpha} e_{xi\alpha} x_{i\alpha} + \tfrac{1}{2}\Sigma_{i\alpha j\beta} f_{xi\alpha j\beta} x_{i\alpha} x_{j\beta} + \cdots \quad , \tag{3}$$

where the $e_{xi\alpha}$ and $f_{xi\alpha j\beta}$ are the Taylor series expansion coefficients, the former being an "effective charge" tensor for the α^{th} ion. The terms in M_x third and higher order in the $x_{i\alpha}$ may be assumed to contribute less to (1) than the quadratic term whenever the quadratic term gives rise to sum-and difference-absorption bands that contribute less to the integral in (1) than does the fundamental absorption line(s) arising from the leading, linear dipole moment, term. (In fact for all potential IR window materials we may neglect higher than quadratic terms in M_x when computing the RHS of (1) to within the experimental errors in determining the LHS).

2. CRYSTALS WITH LINEAR DIPOLE MOMENTS

If the mechanism of anharmonic forces dominates that of the nonlinear moment, we may neglect all but the term linear in $x_{i\alpha}$ in the expression (3) for the dipole moment. Then we need study only the $e_{xi\alpha}$, whose forms depend on the symmetry of the site at $R_{i\alpha}$. For ions at sites having point symmetries T, T_h, T_d, O, or O_h (such as the ions in the alkali halides, GaAs, ZnSe and CdTe),

$$e_{xi\alpha} \rightarrow e_\alpha \delta_{xi} \tag{4}$$

where e_α is called the "effective charge" of the ion α and δ_{xi} is the Kronecker delta. For diatomic cubic crystals such as the aforementioned, the two effective charges must be related by

$$e_1 = -e_2 = e^* \tag{5}$$

in order that no moment developes from (3) when all ions are uniformly translated.

If all the prominent features of $\varepsilon_2(\omega)$ arise from a linear dipole moment, acting with anharmonic interionic forces, in alkali-halide and other diatomic cubic crystals, then we see from (3)-(5) that (1) reduces to

$$\int_0^\infty d\omega\omega\varepsilon_2(\omega) \to 2\pi^2\rho e^{*2}/\mu \ , \tag{6}$$

where ρ is the number density of molecules and $\mu^{-1}=m_\alpha^{-1}+m_\beta^{-1}$ is the molecular reduced mass. In this case, furthermore, the crystal must exhibit a dielectric function ε_2 that obeys (6) at different temperatures and densities, with an essentially invariant effective charge e^*. This can be seen as follows. As the temperature is raised and the crystal expands, the Taylor series (3) for the dipole moment must be re-expressed in powers of the deviations $x_{i\alpha}'$ about the new average ionic positions $R_{i\alpha}' = R_{i\alpha}+\delta R_{i\alpha}$. Substituting

$$x_{i\alpha} = x_{i\alpha}' + \delta R_{i\alpha} \tag{7}$$

in (3) gives for the "effective charge" coefficients of the linear term in the dipole moment expansion, at the new temperature,

$$e_{xi\alpha}' = e_{xi\alpha}+\Sigma_{j\beta} f_{xi\alpha j\beta}\delta R_{j\beta}+\ldots \tag{8}$$

But $\delta R_{j\beta}$ is of the order of, or smaller than, the rms fluctuations in $x_{i\alpha}$. Therefore, if the nonlinear moment term can be neglected in (3), then so can the change in effective charge, proportional to δR, in (8). QED.

3. CRYSTALS WITH NONLINEAR DIPOLE MOMENTS

If the imaginary part of the dielectric constant fails to obey (6), then it can only be because the nonlinear quadratic, or "f",

term in the dipole moment (3) must be contributing to the average in (1). To see what a deviation from (6) means, one must construct a theory for the form of the f - coefficients, and use experimental values of the LHS of (1) to determine the parameters in the theory. Fortunately, the averages over the $(fx)^2$ terms required in (1) can always in principle be performed because, to the desired order of accuracy, the lattice may be assumed to be perfectly harmonic. We illustrate the foregoing procedure by using the independent-molecule model of the lattice that has been used extensively in estimating multi-phonon absorption.[3] In this model, each one-dimensional molecule in the crystal contributes independently to the total dipole an amount

$$m_x = ex + \tfrac{1}{2}fx^2 \tag{9}$$

where x is the deviation from the equilibrium interatomic distance at the temperature under consideration. Equation (1) then reduces to

$$\int_0^\infty d\omega\omega\varepsilon_2(\omega) \to 2\pi^2\rho(e^2 + f^2\langle x^2\rangle)/\mu \ . \tag{10}$$

At another temperature (indicated by primes) the frequency integral becomes

$$2\pi^2\rho' \ [(e + f\delta R)^2 + f^2\langle x'^2\rangle]/\mu \ . \tag{11}$$

The linear expansion δR and densities ρ and ρ' are known, and $\langle x^2\rangle$ is easily calculated for the harmonic oscillator at the two temperatures, assuming its mass to be μ and its frequency to equal ω_{TO}. Therefore the two expressions (10) and (11) can be solved for the two unknowns e and f. Then the contribution to the integral of multi-phonon absorption arising from the nonlinear moment is simply the value of the second term in (10) or (11). Subtracting this value from the total multi-phonon contribution measured gives the anharmonicity contribution to the integral in (10) or (11).

In this manner the multi-phonon absorption mechanisms can be separated with fair accuracy. Introducing more sophisticated forms for M_x than (9) into more realistic lattice models, and using the lattice "shell models" that have been developed to fit neutron scattering data, should give extremely accurate separation of mechanisms once accurate data on $\varepsilon_2(\omega)$ becomes available. However, we believe that even the simple independent-molecule model, used judiciously in (1), can yield a very good picture of the relative importance of the two mechanisms. We now illustrate its use in the following section.

4. APPLICATION TO LITHIUM FLOURIDE

The only crystal for which $\varepsilon_2(\omega)$ has been measured over a wide frequency range at several temperatures is LiF. M. Klier[4] has measured its ε_2 by transmission measurements in the ranges 8 to 14μm and 40 to 400μm, at 300, 22, and -196°C.

Kachare, et al.,[5] have analyzed the reflection data of Jasperse, et al.,[6] by classical dispersion analysis to give values for ε_2 in the range omitted by Kleir and at temperatures 7.5, 85, 295, 420, and 600°K. Kachare (private communication) later verified these results by a Kramers-Kronig analysis. We have interpolated this data to combine it with Klier's and evaluate the integral of (1) at 77, 295, and 573°K.

The results, with number densities from ref. 7, are given in Table 1.

Table I

Temperature (°K)	$10^{-28}\int_0^\infty d\omega\omega\varepsilon_2(\omega)$ sec^{-2}	$10^{-22}\rho$ cm^{-3}
77	3.65	6.20
295	3.64	6.12
573	3.72	5.92

We estimate the experimental accuracy of the integral to be ±1% from the errors estimated in refs. 4 and 5. If this estimate is correct, the experimental results are not quite consistent with a pure linear dipole moment, once the density changes are accounted for. If we solve (11), taking μ to be 8.44×10^{-24}gm (the reduced mass of Li and F), taking the molecular vibration frequency to be the observed fundamental lattice absorption frequency (given in ref. 5 as 317.5, 307.5, and 300 cm^{-1} respectively at the temperatures in Table I), and assuming the values of the integrals in Table I to be exact, we find that the $f^2\langle x^2\rangle$ term contributes 2.2% of the integral at 573°K whereas 10 ± 1% of the integral is observed to arise from multi-phonon absorption. If the measured values for the integrals in Table I were in error so as to underestimate the nonlinear moment effects, we estimate that the $f^2\langle x^2\rangle$ term could contribute as much as a third of the multi-phonon part at 573°K. The values for 295°K suggest that the nonlinear moment is relatively less important at the lower temperatures where the multiphonon contributions are less altogether. (From (10) e=1.04 electron charge.)

In summary, the uncertainties in the data and in the approximations of (10) and (11) probably allow us to conclude no more than that the nonlinear moment gives a minor if not negligible contribution to the multi-phonon absorption in LiF as it is manifested in the integral in (1). We hope that similar measurements will be made in materials like ZnSe, CdTe and GaAs for which the mechanisms are so much more in doubt. The application of the exact relation (1), or approximate forms like (10) and (11), to such data should be able to establish the relative importance of anharmonicities and nonlinear moments to multi-phonon absorption in these materials.

APPENDIX I

According to a well-known quantum mechanical formula (in esu),[7]

$$\epsilon_2(\omega) = 4\pi^2 V^{-1} \Sigma_{m,n} (P_m - P_n) |\langle m|M_x|n\rangle|^2 \delta(\hbar\omega - E_n + E_m) \qquad (A1)$$

where P_m is the probability of the material inside V being in state $|m\rangle$ with energy E_m. Integrating (A1) by $\omega d\omega$ from $-\infty$ to ∞ replaces the δ-function in (A1) by $(E_n - E_m)/\hbar$. Then the P_n terms give the same result as do the P_m, and may be dropped if the latter are doubled. Next, use the identity

$$\Sigma_n (E_m - E_n) |\langle m|M_x|n\rangle|^2 \equiv \tfrac{1}{2}\langle m|[[H, M_x], M_x]|m\rangle \qquad (A2)$$

and then evaluate the commutator using

$$H = \tfrac{1}{2}\Sigma_{i\alpha} p_{i\alpha}{}^2/m_\alpha + U. \qquad (A3)$$

Since both the full lattice potential energy U and M_x are functions of the ion positions only, U does not contribute to the commutator. Using the commutator identity

$$M_x, p_{i\alpha} = i\hbar \partial M_x / \partial x_{i\alpha} \qquad (A4)$$

in (A3) leads then directly to the desired sum rule, equation (1).

ACKNOWLEDGMENT*

*Research sponsored by Defence Advanced Research Projects Agency contract No. F19 628-72-C-0275 monitored by Air Force Cambridge Research Labs.

REFERENCES

1. The best known argument for neglecting the anharmonic moment in alkali-halide crystals is that of P. Keating and G. Rupprecht, Phys. Rev. 138, A866 (1965).

2. There exist a number of theoretical arguments that one, or the

other, or both, mechanisms are important in III-V compounds. See for example, a) D. A. Kleinman, Phys. Rev. 118, 118 (1960); b) D. A. Kleinman and W. G. Spitzer, Phys. Rev. 118, 160 (1960); c) R. Geick, Phys. Rev. 138, A1495 (1965); d) C. Flytzanis, Phys. Rev. Letters 29, 772 (1972). For example, the most recent of these (d) argues that the contributions of the two mechanisms to microwave harmonic generation are of opposite sign, and therefore measurement of the sign of the total contribution determines which contribution is the larger. The theory of the sign of the nonlinear moment's contribution is however uncertain.

3. a) M. Sparks and L. J. Sham, Solid State Comm. 11, 1451 (1972); b) B. Bendow, Phys. Lett. 42A, 359 (1973); c) T. C. McGill, R. W. Hellwarth, M. Mangir, and H. Winston, J. Phys. Chem. Solids (to be published).

4. M. Klier, Zeit, fur Physik 150, 238 (1958).

5. A. Kachare, G. Andermann, and L. R. Brantley, J. Phys. Chem Solids 33, 467 (1972).

6. J. R. Jasperse, A. Kahan, J. N. Plendl and S. S. Mitra, Phys. Rev. 146, 526 (1966).

7. "Compendium on High Power IR Laser Window Materials" by C. Sahagian and C. Pitha (AFCRL Special Report No. 135, LQ-10 Program, 1972).

8. R. A. Cowley, in "Phonons in Perfect Lattices", pp. 170-207 (ed. R. W. H. Stevenson, Plenum Press, New York 1966).

f.1 Wavelength and Temperature Dependent Calorimetry Measurements on GaAs

W. H. Steier, C. P. Christensen, R. Joiner

In the preceding quarter we reported irreversible increases in the absorption of high-resistivity GaAs produced by heating the material in air to a temperature of 400°C. At that time it was evident that both surface and bulk effects contributed to the observed change in room-temperature absorption. Attempts to determine the thickness of the highly-absorbing surface layer by use of controlled chemical polishing or etching have been unsuccessful due to formation of an opaque surface film during the polishing or etching process when less than 5μ - 10μ of material is removed. It has been found, however, that a cleaning process using the organic solvents trichlorethylene, acetone, and methyl alcohol, followed by wiping the surfaces with a soft swab or cloth is sufficient to remove a sizable fraction of the absorbing surface layer.

The absorption mechanism in the surface layer is not well understood. It seems quite possible that oxides of arsenic, which are known to possess fundamental vibrations with frequencies as high as 1200 cm^{-1}(1) are responsible for the observed loss. However, an attempt to measure surface oxygen concentration by electro-chemical techniques with the assistance of Professor J. M. Whelan was inconclusive.

Bulk absorption in samples subjected to several thermal cycles has been found to increase after each heating. Bell Laboratories sample 55-1A, described in the previous report, showed an increase in bulk absorption from .006 cm^{-1} to .018 cm^{-1} after four successive 400°C heating cycles. However, the increased bulk absorption was not accompanied by significant changes in electrical properties. Resistivity and Hall measurements made after the heating cycles yielded $\rho = 2.8 \times 10^8$ Ω-cm and $\mu_H = 3350$ $cm^2/v\text{-}sec$. Comparison with Bell Labs data on similar samples (Quarterly Report #4) shows a possible factor of two reduction in mobility to be the only effect of heating as far as electrical parameters are concerned. The irreversible changes caused by heating are thus

still a mystery.

The temperature dependence of multiphonon absorption in GaAs near 10μ has been calculated using the formulas of McGill et al.[2], and Bendow[3]. Using the experimental results of Chang et.al.[4] and Horrigan and Deutsch[5] to obtain the necessary constants, we find good agreement between experiment (Q.R. #5) and theory for temperatures below 280°C. However, it is clear that other absorption mechanisms could also exhibit the observed weak temperature dependence in the temperature range.

Absorption spectra for two additional samples have been obtained in a continuation of our GaAs evaluation program. Sample 44-3A, a carbon-doped crystal obtained from Bell Laboratories (see Q.R. #4 for resistivity and mobility), exhibited an absorption spectrum nearly identical to the other very low-loss samples that have been measured (55-1A, WA-1000, WORM-1). A second high resistivity sample, doped with Si and Cr, was obtained from Hoboken Laboratories of Belgium and showed an absorption spectrum very similar to sample EMC 6050T reported previously.

We note that the four lowest-loss samples in the evaluation program representing widely different growth and comparison techniques, exhibit nearly identical absorption spectra. This suggests that absorption in the best currently available GaAs may be limited by an intrinsic loss mechanism. However, the observed irreversible heating effects require explanation if this hypothesis is to hold. Experiments are now in preparation which will allow annealing of samples in a controlled atmosphere. These experiments should provide further information on the origin of the irreversible effects.

References

1. N. N. Soboleo and V. P. Cheremisinov, Optics and Spectroscopy, 9, 233 (1960)

2. T. C. McGill, R. W. Hellwarth, M. Mangir, and H. V. Winston (to be published)

3. B. Bendow, Appl. Phys. Lett. 23, 133 (1973)

4. R. K. Chang, J. M. Ralston, and D. E. Keating, Proceedings of the International Conference on Light Scattering Spectra of Solids, New York University, 1968; p. 369

5. F. A. Horrigan and T. F. Deutsch, Raytheon Research Div. Quarterly Technical Reports, Nos. 1 and 2, Contract No. DA-AH01-72-C-0194, 1972.

f.2 Alkali Halide Surface Studies with Acoustic Probe Techniques

J. H. Parks, D. A. Rockwell, T. Colbert

During this quarter we successfully demonstrated that a fluid coupling process [1] could be used to transfer surface acoustic waves from crystalline quartz onto non-piezoelectric KCl. The establishment and control of this technology allowed us to make the first measurements of 10.6μ absorption in KCl samples using the techniques of acoustic temperature detection.

f.2a Fluid Coupling of Acoustic Surface Waves

Initial fluid coupling experiments indicated that several liquids could be useful. These included water, xylene, and a eutectic Ga:In binary alloy. Xylene was chosen as the coupling fluid for KCl on the basis of minimum phase drift and coupling stability. The coupling technique is illustrated in Figure 1. The transmitting and receiving transducers were constructed on a single piece of quartz to insure proper orientation and positioning with respect to each other. The KCl samples were obtained from Janos Optical Corp. and had a single surface optically polished to allow propagation of the acoustic surface wave. An RF signal of 120 MHz and 500 mV rms was applied to the transmitting transducer and ~1 mV rms signal was detected at the receiving transducer. This low coupling efficiency is due to the acoustic impedance mismatch at the fluid coupling interfaces. This could be increased somewhat if we replaced quartz with another piezoelectric material having acoustic properties closer to those of KCl, such as Bismuth-Germanum-Oxide (BGO). The important point, however, is that the coupling technique does perform adequately and the received signal is of sufficient strength to allow accurate determination of the surface wave phase change induced by the absorbed 10.6μ radiation.

f.2b Experimental Results and Preliminary Analysis

The data recordings presented in the following figures were taken with the experimental arrangement shown in Figure 2. Figure 3 shows typical results for our KCl samples. These data

were reproducible for different samples and were insensitive to changes of the coupling fluid. The strip chart recording shows the phase variation of the surface wave vs. time, when three successive 10.6μ laser pulses of 1 second duration were incident on the KCl sample. We note a rapid increase in the phase value of $\Delta\phi_1$, during the time of the laser pulse, and then a decay to a value $\Delta\phi_2$ above the initial level after the 10.6μ pulse ends. This step-like behavior was consistently observed when the sample was irradiated by successive 10.6μ pulses. Figures 4 and 5 show the variation of $\Delta\phi_1$ and the average slope $\frac{\Delta\phi}{\Delta t}$ with laser pulse energy at a constant pulsewidth of 1 second.

Figure 6 shows the variation of the ratio $\Delta\phi_1/\Delta\phi_2$ with the pulse duration. The fact that this ratio was found to decrease to 1 for longer pulses indicates the presence of some "grow-in" process. This could be the result of thermal diffusion bringing the acoustically probed region to equilibrium with the remainder of the sample, or the onset of effects due to the constrained state of the irradiated region. The thermal spatial gradiant caused by the 10.6μ beam will induce stresses in the sample which tend to constrain thermal expansion in the heated region during the laser pulse. When the pulse ends, diffusion will begin to reduce this gradiant and thermal expansion will proceed. Since the phase shift is sensitive to the acoustic path length, it may be indicating an actual <u>increase</u> in magnitude due to this expansion. These possibilities necessitate the derivation of a more accurate relationship between the temperature change and the resulting phase variation which would include the effects of diffusion and thermoelastic stress. This theory has been completed and is being applied to data analysis at the present time.

<u>f.2c Research Plans</u>

In order to minimize the effects of thermal diffusion, we will attempt acoustic probe measurements with shorter laser pulses, perhaps as short as a few milliseconds. In this time the diffusion process will tend to thermalize only material within the acoustic energy volume which for propagation on KCl

is ~70μ deep. This will require laser powers as high as 50 - 75 watts, based on sensitivity results of our current measurements. This source is presently being constructed.

We will apply our technique to absorption measurements of several samples grown at Hughes-Malibu laboratories. These will include RAP-grown KCl with polished and HCl etched surfaces and also polycrystalline samples. These experiments will indicate the sensitivity of these acoustic measurements to surface quality and will supplement results reported by other groups on similiar materials and surfaces.

We are also preparing an interdigital transducer pair which will allow probe measurements on KCl at the first and third harmonic RF frequencies with equal efficiency during the same experimental run. In this way, the experimental parameters can be kept identical for two acoustic probe depths differing by a factor of 3. These experiments may indicate the presence of differing bulk and surface properties.

1. F. A. Kroger, J. H. Margurger et al., Electronic Sciences Laboratory, University of Southern California, "IR Window Studies," Quarterly Technical Report No. 5 (June - August 1973) AFCRL TR-73- Contract No. F19628-72-C-0275, ARPA Order No. 2055.

2. ibid., Report No. 3 (December - February 1973) AFCRL TR-73-0325, Contract No. F19628-72-C-0275, ARPA Order No. 2055 (29 September 1972).

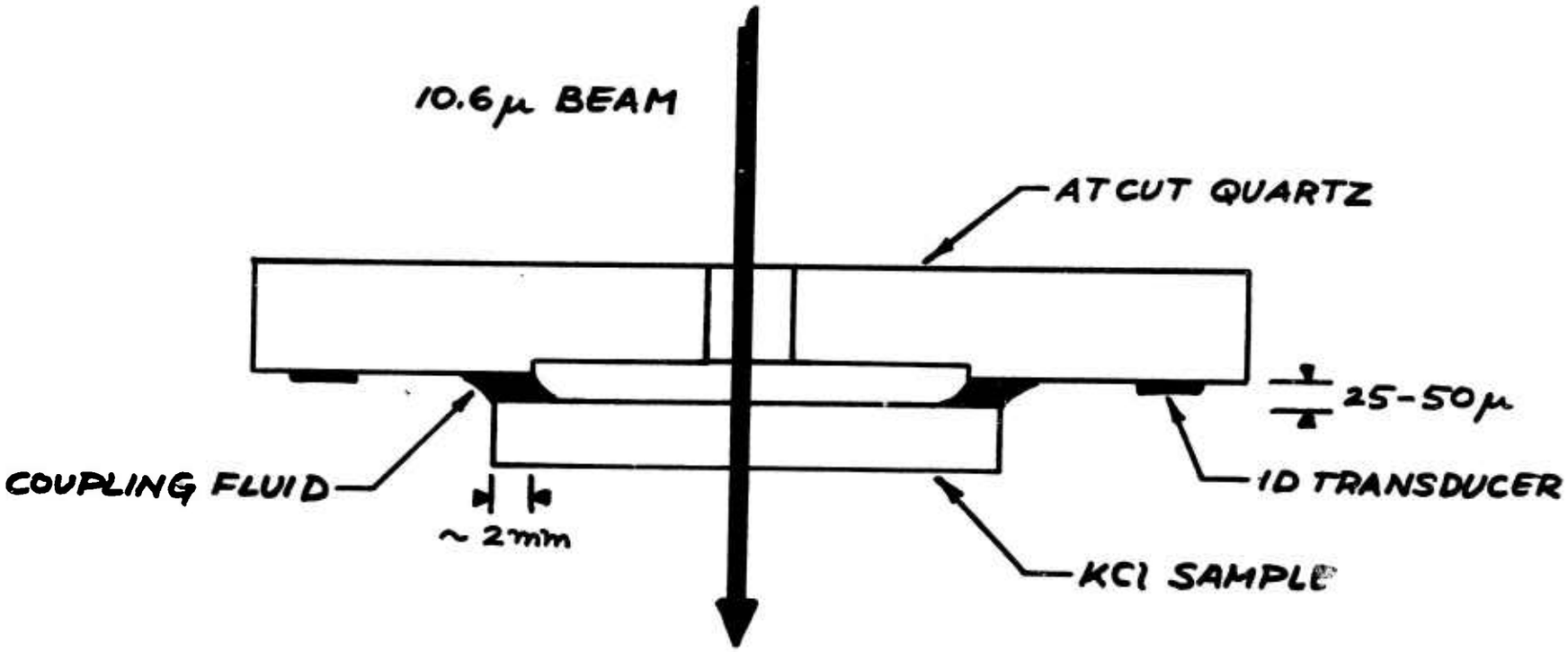

FLUID COUPLING TECHNIQUE

- H_2O
- XYLENE, 500mv → ~1mv, DRIFT < 2mrad/sec
- Ga-In EUTECTIC BINARY ALLOY

Figure 1

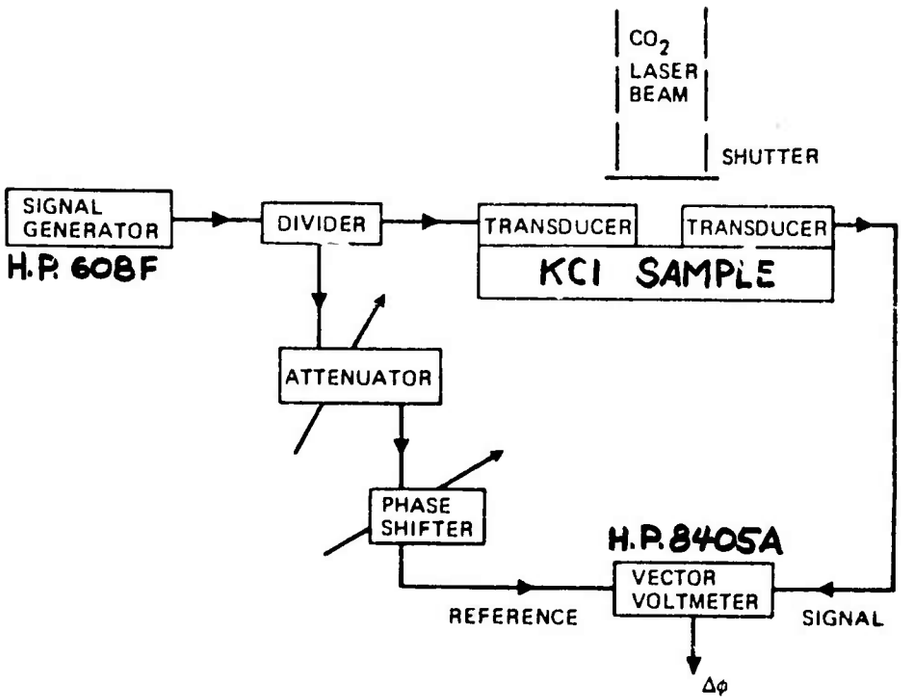

FIG. 2 General Experimental Arrangement for Reading the Temperature Induced Change in Output Phase, $\Delta\phi$, Brought About by the Absorption of a CO_2 Laser Beam.

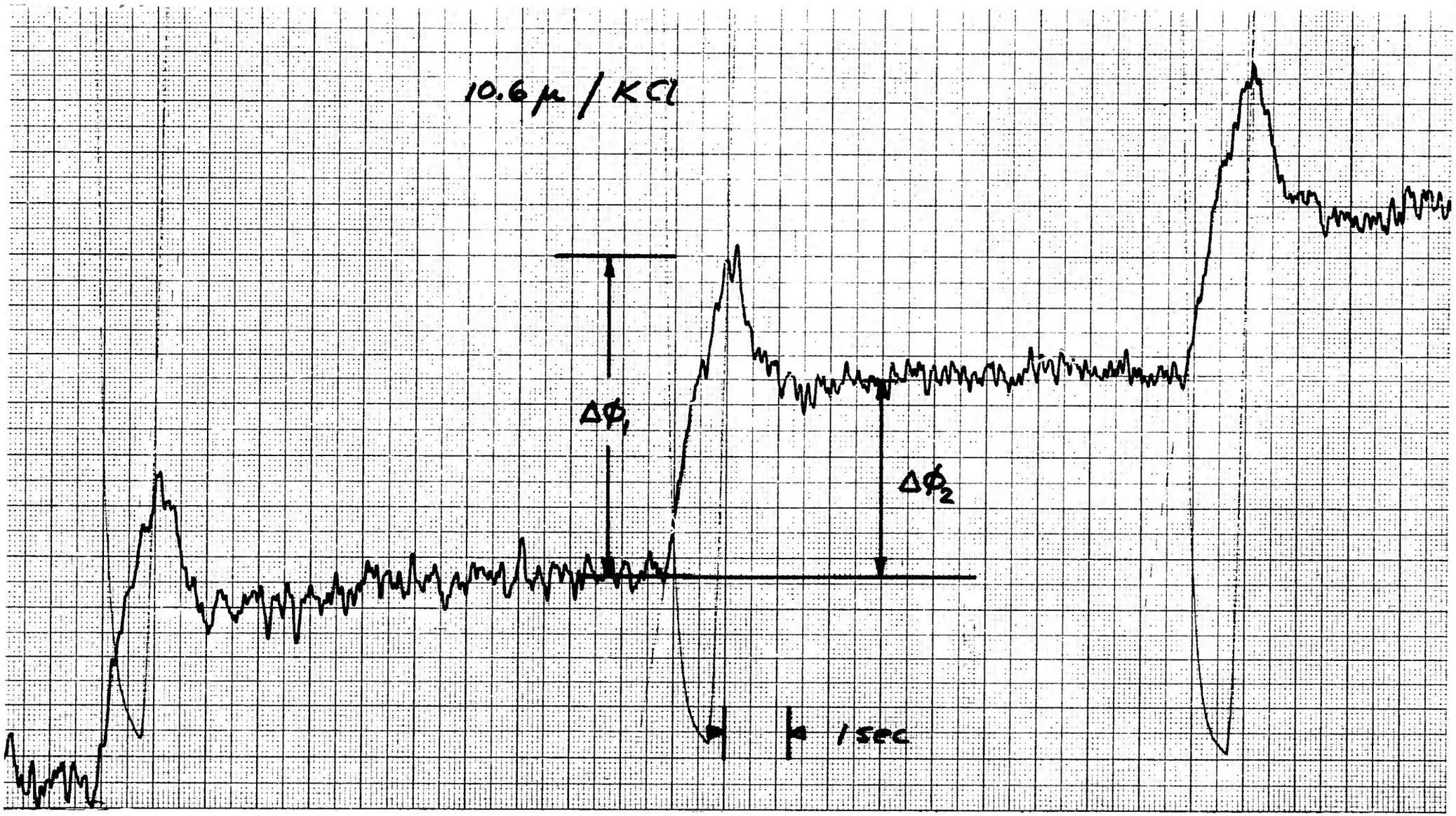

Figure 3

Figure 4

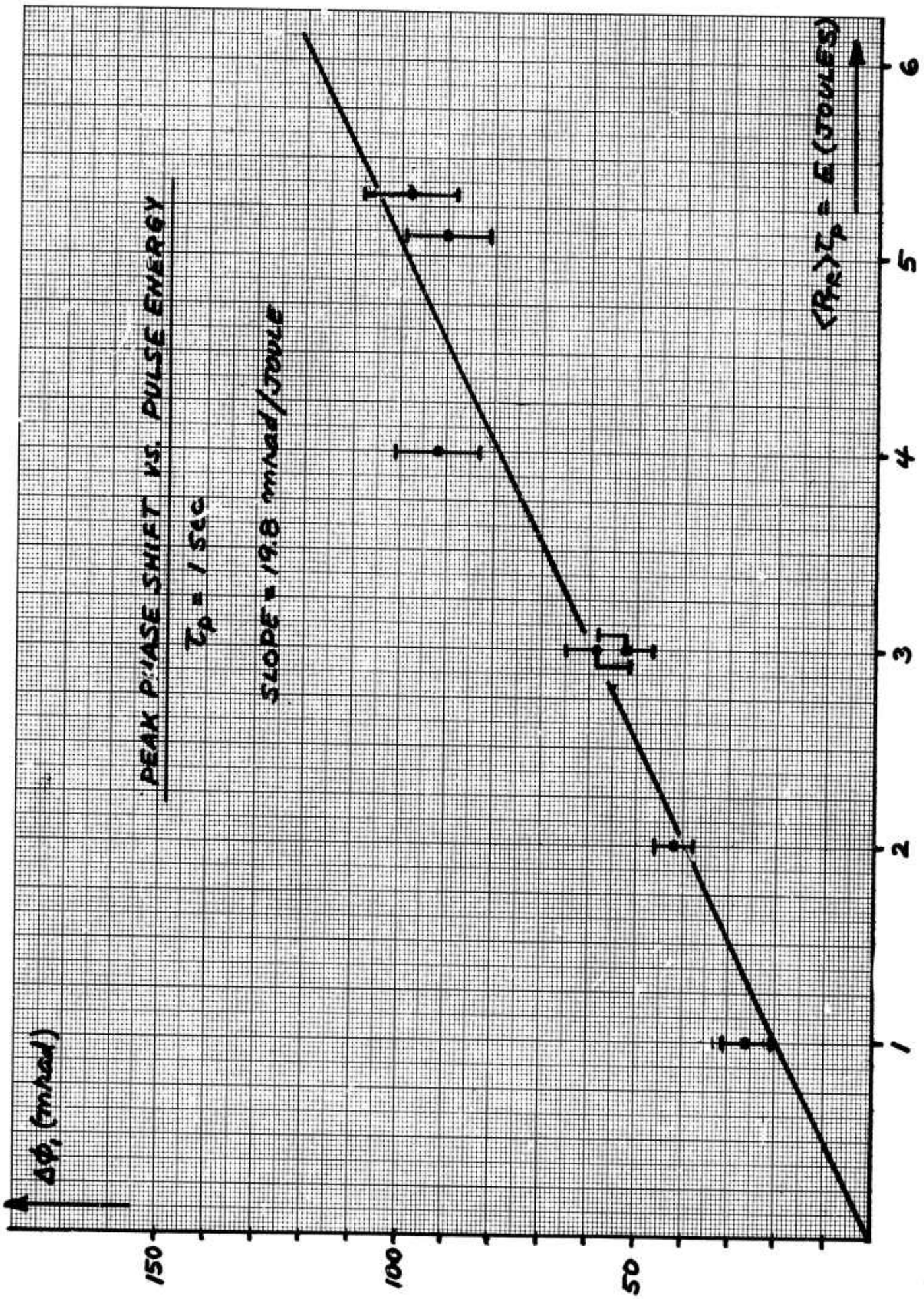
PEAK PHASE SHIFT VS. PULSE ENERGY
T_p = 1 sec
SLOPE = 19.8 mrad/JOULE
$\Delta\phi$, (mrad)
150
100
50
1
2
3
4
5
6
$\langle P_R \rangle T_p$ = E (JOULES)

Figure 5

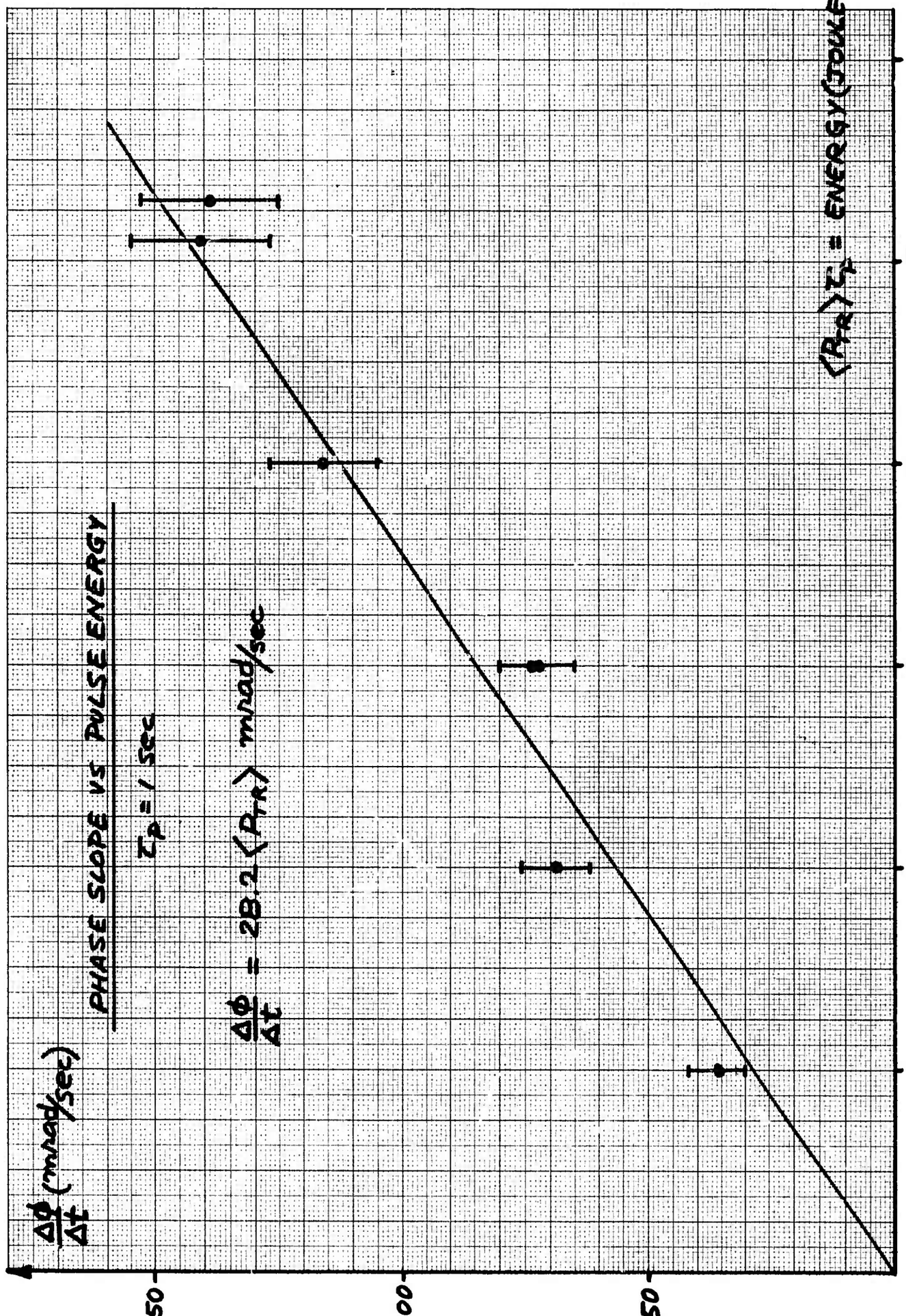
PHASE SLOPE VS PULSE ENERGY
$\tau_p = 1$ sec
$\frac{\Delta\phi}{\Delta t} = 28.2\langle P_{FR}\rangle$ mrad/sec
$\frac{\Delta\phi}{\Delta t}$ (mrad/sec)
150
100
50
1
2
3
4
5
6
$\langle P_{FR}\rangle \tau_p$ = ENERGY (JOULES)

Figure 6

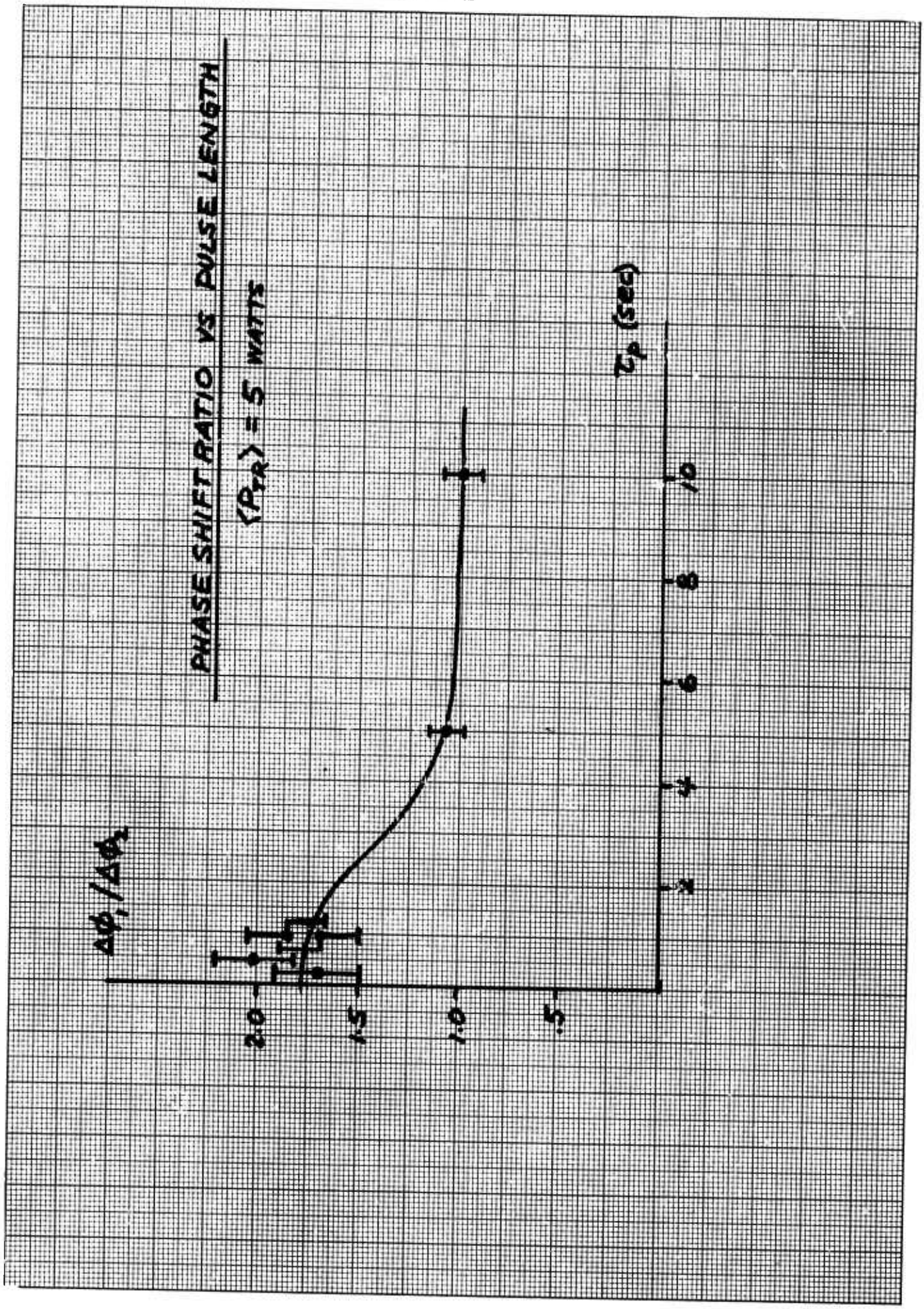
PHASE SHIFT RATIO VS PULSE LENGTH
$\langle P_{TR} \rangle$ = 5 WATTS
$\Delta\phi_1 / \Delta\phi_2$
τ_p (sec)
2.0
1.5
1.0
.5
10
8
6
4
2

g.1 Characterization of Optical Performance of IR Window Systems

J. H. Marburger, Martin Flannery

With this quarterly report, we begin an extensive review of the theory of thermal lensing, which summarizes work performed on this contract, and also includes results first obtained by others, e.g. Bendow and Gianino at AFCRL.[1] This review, which will be published elsewhere when complete, differs somewhat in viewpoint from previous work, and stresses physical interpretation of the formalism.

1. The Diffraction Integral for Beams

The starting point for all diffraction computations in this work is the slowly varying envelope equation for the complex optical field envelope $\vec{E}$, which is related to the optical electric field $\vec{E}_{opt.}$ through

$$\vec{E}_{opt} = \text{Re } \vec{E} e^{i(kz - \omega t)} . \tag{1.1}$$

Here z is the direction of propagation of the beam under consideration, and $k = n\omega/c$, n being the refractive index of the propagation medium (air) at the dominant frequency ω of the beam. Because spatial variations along the beam direction are supposed to occur over distances large compared to $\lambda = 2\pi/k$, we have

$$\left|\frac{\partial^2 \vec{E}}{\partial z^2}\right| << \left|k\frac{\partial \vec{E}}{\partial z}\right| , \left|\frac{\partial^2 \vec{E}}{\partial t^2}\right| << \left|\omega\frac{\partial \vec{E}}{\partial t}\right| . \tag{1.2}$$

Under these conditions, Maxwell's equations for propagation in a linear isotropic homogeneous medium imply

$$2ik\left(\frac{\partial \vec{E}}{\partial z} + \frac{1}{v_g}\frac{\partial \vec{E}}{\partial t}\right) + \nabla_T^2 \vec{E} = 0 \tag{1.3}$$

Here v_g is the group velocity, and we have ignored group velocity dispersion. ∇_t^2 is the transverse laplacian

$$\nabla_T^2 = \frac{\partial^2}{\partial x^2} + \frac{\partial^2}{\partial y^2} .$$

With the change of variable $\tau = t - z/v_g$, eqn. (1.3) becomes

$$2ik \frac{\partial \vec{E}}{\partial z} + \nabla_T^2 \vec{E} = 0 \tag{1.4}$$

where $\vec{E}$ is now a function of x, y, z and τ. Since this equation does not depend on τ, all time dependence is contained in the initial condition, which we write as

$$\vec{E}_o(x,y,t) = \vec{E}(x,y,o,t). \tag{1.5}$$

The general solution of (1.4) with initial condition (1.5) is

$$\vec{E}(\vec{r},z) = \frac{-ik}{2\pi z} \iint d^2r' e^{i\frac{k}{2z}(\vec{r} - \vec{r}')^2} \vec{E}_o(\vec{r}') \tag{1.6}$$

where the t dependence is suppressed, and $\vec{r} = (x,y)$. If $\vec{E}_o$ is derived from a field $\vec{E}_1$ which passes through a thin positive lens of focal length R at $z = 0$, then $\vec{E}_o$ may be replaced in (1.6) by

$$\vec{E}_o = \vec{E}_1 \exp -ikr^2/2R . \tag{1.7}$$

The incident beam $\vec{E}_1$ is usually limited by an aperture of characteristic dimension d, which is a convenient scaling length for the transverse variables. The near field length of the aperture, kd^2, is a convenient scaling length for longitudinal variables. Introducing

$$\vec{\rho} \equiv \vec{r}/d, \quad \zeta \equiv z/kd^2, \quad \rho = R/kd^2, \tag{1.8}$$

we find that the diffraction integral is

$$\vec{E}(\vec{\rho},\zeta) = \frac{1}{2\pi i} \frac{1}{\zeta} e^{i\rho^2/2\zeta} \iint d^2\rho' K(\vec{\rho},\vec{\rho}',\zeta) \vec{E}_1(\vec{\rho}') \tag{1.9}$$

where

$$K(\vec{\rho},\vec{\rho}',\zeta) \equiv \exp i\left[\frac{\rho'^2}{2}\left(\frac{1}{\zeta} - \frac{1}{\rho}\right) - \frac{\vec{\rho}\cdot\vec{\rho}'}{\zeta}\right] . \tag{1.10}$$

The variables ρ and ζ are somewhat more easily visualized than the conventional u, v variables employed by Born and Wolf,[2] and Bendow et al.[1]

$$u = kd^2\left(\frac{1}{R} - \frac{1}{z}\right) = \frac{1}{\rho} - \frac{1}{\zeta} \tag{1.11}$$

$$v = \frac{kd^2 r}{z} = \frac{\rho}{\zeta} . \tag{1.12}$$

The diffraction kernel K is simpler in appearance in the variables u and v, but for complicated diffraction fields, it is useful to employ variables like $\vec{\rho}$, ζ which are directly proportional to transverse and longitudinal distances, with constant scale factors. We use both sets of variables to make intermediate formulas more concise, but all graphs and interpretations will involve only ρ and ζ.

2. Vector Corrections

The slowly varying envelope equation (1.3) is satisfied by field vectors whose polarization remains parallel to the plane of incidence. But the transversality condition $\nabla \cdot \vec{E}_{opt} = 0$ for the exact optical field requires that the local plane of polarization be tangent to the local wave front, or normal to the rays. Thus $\hat{z} \cdot \vec{E}_{opt}$ must be proportional to $\sin\alpha$, where α is the angle between the local ray direction and the z axis. This is on the average less than d/R, the inverse of twice the f number of the window system. Thus $\alpha = .1$ for an f5 system. This angle must be small for the slowly varying envelope approximation to be accurate, so the error incurred in setting $\hat{z} \cdot \vec{E} = 0$ is small. It is nevertheless useful sometimes to know the magnitude of the longitudinal field (e.g. near a focus). This is very nearly equal to the z component of the projection of $\vec{E}$ on the plane normal to the local ray direction $\hat{n}$. That is, the field

$$\vec{E}_T = (I - \hat{n}\hat{n})\vec{E} ,$$

is a good approximation to the transverse optical field amplitude in the context of the slowly varying envelope approximation. The vector correction $-\hat{n}(\hat{n} \cdot E)$ is ignored in what follows.

3. The Aberration Matrix for Thin Windows

The initial field $\vec{E}_1$ of interest in window studies is the field at the exit plane of the window. This exit field may be obtained from the field $\vec{E}_i$ incident on the window by solving the inhomogeneous envelope equation

$$2ik_1 \frac{\partial \vec{E}}{\partial z} + \nabla_T^2 \vec{E} = -\frac{4\pi\omega^2}{c^2} \vec{\vec{\chi}} \cdot \vec{E} \qquad (3.1)$$

in the window region $-w \leq z \leq 0$. Here $k_1 = n_1 \omega / c$, and n_1 is the mean scalar refractive index of the window. This equation includes the linear, inhomogeneous, possibly anisotropic susceptibility $\vec{\vec{\chi}}$ of the window system. If the window thickness w is less than the scale of variation of $\vec{\vec{\chi}}$, and also less than the shortest diffraction length of any intensity or phase fluctuation in the incident beam, then the approximate solution of (3.1), ignoring reflections at the surfaces, is

$$\vec{E}(\vec{r},0) \approx \left[\exp\left(i2\pi k_1 w \vec{\vec{\chi}}(\vec{r})/n_1^2\right)\right] \cdot \vec{E}(\vec{r},-w) . \qquad (3.2)$$

$$\equiv \vec{\vec{A}}(\vec{r}) \cdot \vec{E}(\vec{r},-w)$$

The quantity $\vec{\vec{A}}(\vec{r})$ will be called the aberration matrix for a thin window. If any of the assumptions leading to (3.2) are violated, we have a thick window, for which the analysis is much more complicated and will not be treated in this report. (The no-reflection assumption is independent of window thickness and will be discussed later.)

The goal of thin window theory is to compute the 2x2 matrix $\vec{\vec{\chi}}(\vec{r})$ from the known properties of the incident beam and the medium, and to determine the influence of these properties on the diffracted field $\vec{E}(\vec{r},z)$ beyond the window. Figure (3.1) shows the geometry of our window model.

4. Aberration Matrix for Cylindrical Anisotropy and Inhomogeneity (Thin Windows)

An important class of window problems has aberration matrices which are diagonal in a cylindrical basis:

$$\vec{\vec{A}}(\vec{r}) = A_r(r)\hat{e}_r\hat{e}_r + A_\theta(r)\hat{e}_\theta\hat{e}_\theta . \qquad (4.1)$$

Fig. 3.1

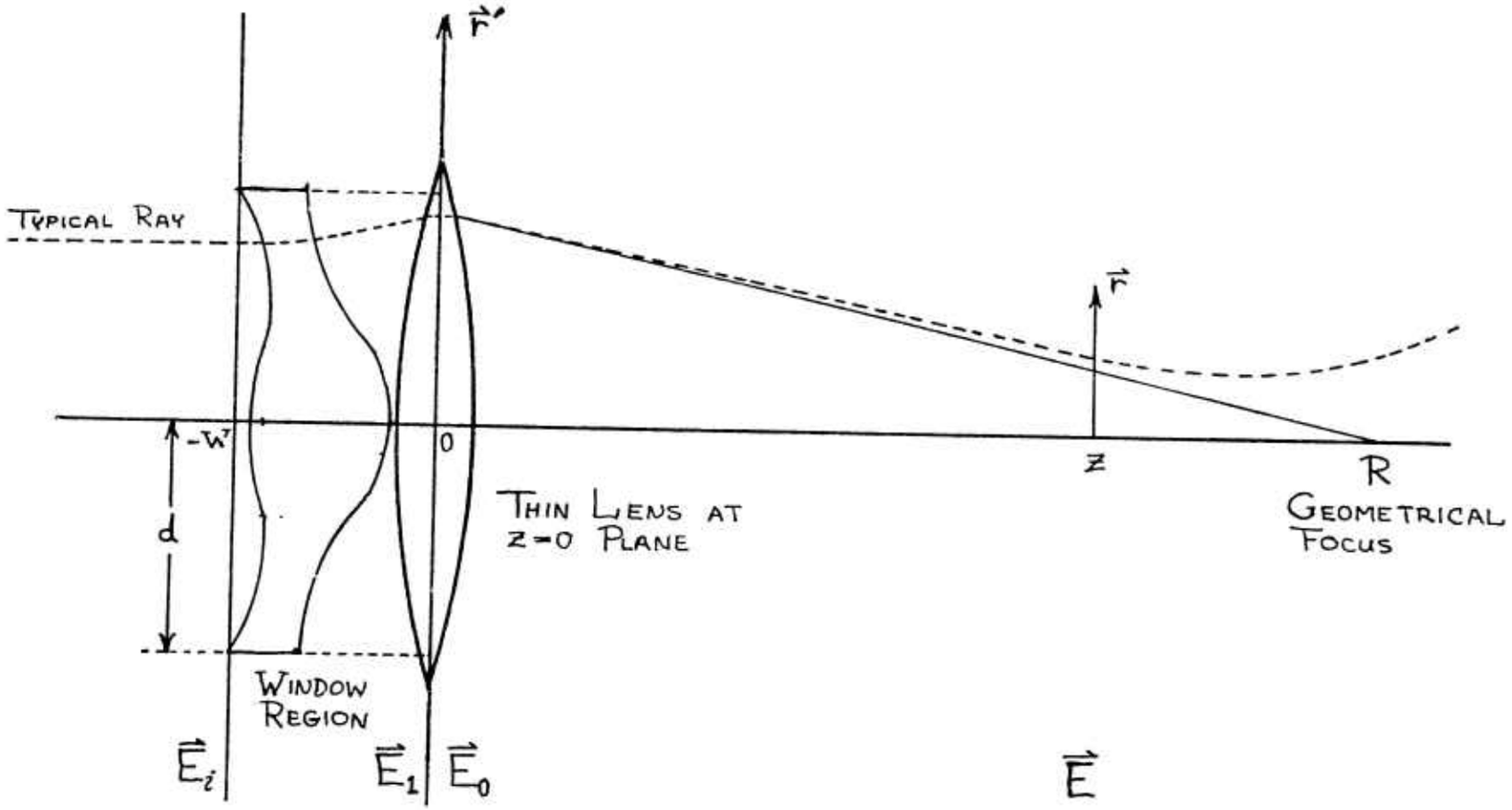

Coordinate system and definitions of fields. $\vec{E}_i$ is the unfocused incident field, and $\vec{E}_1$ the aberrated field after passing through the window. $\vec{E}_0$ is the focused aberrated field at z=0 and $\vec{E}$ the field at z>0. $\vec{r}'$ or r', θ' locates points in the z=0 plane and $\vec{r}$ or r, θ locates points in the z plane. Formulas are usually simpler in the variables $\rho = r/d$, $\zeta = z/kd^2$ where d is the window radius.

Here $\hat{e}_r$ and $\hat{e}_\theta$ are radial and azimuthal unit vectors, and A_r, A_θ are the local eigenvalues of the aberration matrix. Some important properties of $\vec{\vec{A}}$ are:

$$\begin{aligned}
&\vec{\vec{A}}^T = \vec{\vec{A}}, \qquad \vec{\vec{A}}\cdot\vec{\vec{A}}^\dagger = \vec{\vec{I}} \\
&\mathrm{Tr}\vec{\vec{A}} = A_r + A_\theta, \qquad \det \vec{\vec{A}} = A_r A_\theta \\
&\vec{\vec{A}}\cdot\vec{\vec{A}} = (\mathrm{Tr}\vec{\vec{A}})\vec{\vec{A}} - (\det A)\vec{\vec{I}} \quad .
\end{aligned} \tag{4.2}$$

One usually works in a cartesian basis if the incident field is linearly polarized. In this basis,

$$\begin{aligned}
\vec{\vec{A}} &= \begin{pmatrix} A_{xx} & A_{xy} \\ A_{yx} & A_{yy} \end{pmatrix} \\
&= \begin{bmatrix} A_r \cos^2\theta + A_\theta \sin^2\theta & (A_r - A_\theta)\sin\theta\cos\theta \\ (A_r - A_\theta)\sin\theta\cos\theta & A_r \sin^2\theta + A_\theta \cos^2\theta \end{bmatrix}
\end{aligned} \tag{4.3}$$

where r, θ are the polar coordinates of the point in the window at which A_r A_θ are evaluated.

Since $\vec{\vec{A}}$ is unitary, its eigenvalues may be written, (in the notation of Bendow and Gianino[1]),

$$\begin{aligned}
A_r &= \exp ik_1\Phi_r(r) \\
A_\theta &= \exp ik_1\Phi_\theta(r)
\end{aligned} \tag{4.4}$$

If we introduce the mean and difference phases through

$$\begin{aligned}
\phi &\equiv \tfrac{1}{2}k_1(\Phi_r + \Phi_\theta) \\
\Delta &\equiv \tfrac{1}{2}k_1(\Phi_r - \Phi_\theta),
\end{aligned} \tag{4.5}$$

we find the following convenient form for $\vec{\vec{A}}$:

$$\vec{\vec{A}} = e^{i\phi}\begin{bmatrix} \cos\Delta + \sin\Delta\cos 2\theta & \sin\Delta\sin 2\theta \\ \sin\Delta\sin 2\theta & \cos\Delta - \sin\Delta\cos 2\theta \end{bmatrix} . \qquad (4.6)$$

$$= e^{i\phi}\vec{\vec{B}} .$$

If the window is isotropic, $\Delta = 0$, $\vec{\vec{B}} = \vec{\vec{I}}$, and $\vec{\vec{A}} = \vec{\vec{I}} e^{i\varphi}$. (4.7)

Explicit formulas for Δ and φ will be derived in subsequent sections for specific window models. Cylindrical anisotropy generally requires that all stresses and heat sources within the window be distributed with cylindrical symmetry so that the local principal polarizations are radial and azimuthal.

5. Diffraction Field for Cylindrical Anisotropy

The aberration matrix allows us to find the field $\vec{E}_1$ in the diffraction integral (1.9) in terms of the unfocussed field $\vec{E}_i = \vec{E}(\vec{r}, -\vec{w})$ incident on the window. Denoting the difference in azimuth between source point and field point by $\psi = \theta' - \theta$, we may rewrite eqn. (1.9) as

$$\vec{E}(\vec{\rho}, \zeta) = \frac{1}{2\pi i\zeta} \exp\left(\frac{i\rho^2}{2\zeta}\right) \times$$

$$\times \int_0^1 \rho' d\rho' \exp(-\tfrac{1}{2}iu\rho'^2) \exp(i\phi)\mathcal{B}\vec{E}_i(\rho') , \qquad (5.1)$$

where

$$\mathcal{B} = \int_0^{2\pi} d\psi \exp(-iv\rho'\cos\psi)\vec{\vec{B}}(\rho', \theta')$$

$$= \begin{bmatrix} J_o\cos\Delta - J_2\sin\Delta\cos 2\theta & -J_2\sin\Delta\sin 2\theta \\ -J_2\sin\Delta\sin 2\theta & J_o\cos\Delta + J_2\sin\Delta\cos 2\theta \end{bmatrix} . \qquad (5.2)$$

Here J_o and J_2 are Bessel functions whose arguments are $v\rho' = \rho\rho'/\zeta$, and θ is the azimuth of the field point at (ρ, ζ).

The dependence of $\vec{E}(\vec{\rho}, \zeta)$ on θ is explicitly displayed in the matrix (5.2). To discuss this dependence, it is convenient to rewrite the diffraction field in the concise form

$$\vec{E}(\rho,\theta,\zeta) = \vec{E}_o(\rho,\zeta) - \vec{\vec{R}}(\theta)\cdot\vec{E}_2(\rho,\zeta) \tag{5.3}$$

where

$$\vec{\vec{R}}(\theta) = \begin{bmatrix} \cos 2\theta & \sin 2\theta \\ \sin 2\theta & -\cos 2\theta \end{bmatrix} \tag{5.4}$$

$$\vec{E}_o(\rho,\zeta) = \frac{1}{2\pi i\zeta} e^{i\rho^2/2\zeta}\int_0^1 \rho'\, d\rho'\, e^{-\frac{1}{2}iu\rho'^2}\, e^{i\phi}\cos\Delta\, J_o\, \vec{E}_i \tag{5.5}$$

$$\vec{E}_2(\rho,\zeta) = \frac{1}{2\pi i\zeta} e^{i\rho^2/2\zeta}\int_0^1 \rho'\, d\rho'\, e^{-\frac{1}{2}iu\rho'^2}\, e^{i\phi}\sin\Delta\, J_2\, \vec{E}_i \tag{5.6}$$

The matrix $\vec{\vec{R}}$ is its own inverse, so the intensity is proportional to

$$|\vec{E}(\rho,\theta,\zeta)|^2 = |\vec{E}_o|^2 + |\vec{E}_2|^2 - 2\,\mathrm{Re}\,\vec{E}_o\cdot\vec{\vec{R}}(\theta)\cdot\vec{E}_2^* \tag{5.7}$$

This important result shows that <u>the intensity distribution beyond the window is not cylindrically symmetric</u> for a general incident polarization. The actual angular shape of the intensity distribution depends upon the incident polarization state and also upon the relative phases of $\vec{E}_o$ and $\vec{E}_2$. Notice that for an isotropic window (no stress induced birefringence) $\Delta = 0$, $\vec{E}_2 = 0$, and

$$|\vec{E}(\rho,\theta,\zeta)|^2 = |\vec{E}_o(\rho,\zeta)|^2 ,$$

Therefore the departure from cylindrical symmetry in the diffraction field is caused by anisotropy (e.g. stress induced birefringence).

6. Diffracted Beam Geometry for Specific Incident Polarization States

Eqn. (5.7) for the intensity beyond the window may be evaluated to determine the explicit angular dependence for specific incident polarization states. Simple results are obtained only if the incident polarization is the same for all points in the window plane. (e.g. linear polarized in same direction at center as in periphery). In this case $\vec{E}_i$ may be written

$$\vec{E}_i = E_i \left[e^{i\frac{1}{2}\gamma} \cos\eta \, \hat{e}_x + e^{-i\frac{1}{2}\gamma} \sin\eta \, \hat{e}_y \right] \tag{6.1}$$

where E_i is a function of r' or ρ' alone, and the quantities γ, η are related to the orientation angle Ψ and ellipticity ε (ratio of minor to major axis) of the incident polarization ellipse through

$$\begin{aligned} \tan 2\Psi &= \tan 2\eta \cos\gamma \\ \varepsilon &= \tan\chi \\ \sin 2\chi &= \sin 2\eta \sin\gamma \, . \end{aligned} \tag{6.2}$$

Because the incident orientation is irrelevant, we shall take $\Psi = 0$ in the following.

The computation of $\vec{E}_o \cdot \vec{\vec{R}} \cdot \vec{E}_2^*$ is now straightforward. After some trigonometry, one finds

$$\vec{E}_o \cdot \vec{\vec{R}}(\Theta) \cdot \vec{E}_2^* = E_o E_2^* \cos 2\chi \cos 2\Theta \tag{6.3}$$

where E_o and E_2 are obtained from (5.5) and (5.6) by replacing $\vec{E}_i$ by E_i. The angular distribution

$$|\vec{E}(\rho, \Theta, \zeta)|^2 = |E_o|^2 + |E_2|^2 - 2(\mathrm{Re}\, E_o E_2^*) \cos 2\chi \cos 2\Theta \tag{6.4}$$

Fig. 6.1

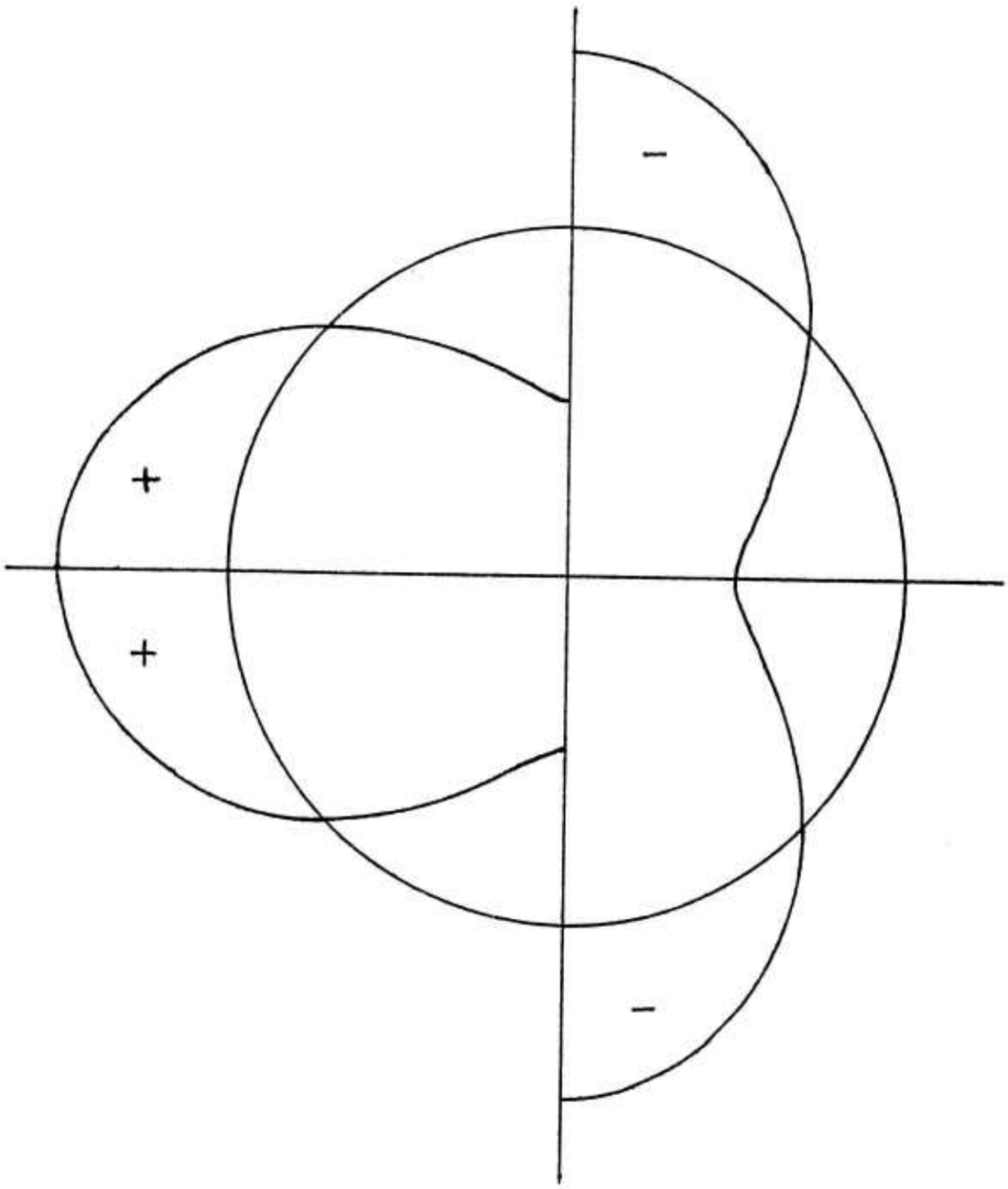

Angular plot of intensity at fixed r, z for linear polarization and $E_o E_2^* = \pm |E_o E_2|$. These curves resemble but are not actually the constant intensity contours, which are sensitive to the detailed dependence of E_o, E_2 on radius. For the curves shown, $|E_2| / |E_o| \approx .2$. The radius of the circle is the unmodulated intensity $|E_o|^2 + |E_2|^2$.

therefore oscillates between the shapes plotted in Figure (6.1) as the relative phase of E_o and E_2 changes. The angular modulation is most severe for linear incident polarization ($2\chi = 0$), and vanishes for circular polarization ($2\chi = \pm \pi/2$). Cylindrical symmetry is also preserved for unpolarized incident light, for which the diffraction field is an incoherent superposition of all possible polarization states. Thus

$$|\vec{E}|^2 = |E_o|^2 + |E_2|^2 \quad \text{(unpolarized, circularly polarized)} \qquad (6.5)$$

$$|\vec{E}|^2 = |E_o|^2 + |E_2|^2 - 2(\mathrm{Re}\ E_o E_2^*)\cos 2\theta \quad \text{(linearly polarized)} \qquad (6.6)$$

7. Relation to Notation of Bendow and Gianino

Bendow and Gianino[1] decompose $\vec{E}$ into cartesian components, and define $\vec{U}$ through

$$\vec{U} = (2\pi i\zeta)\exp(-i\rho^2/2\zeta)\vec{E} \equiv b\vec{E}$$

to remove the initial factor in (5.1). The components of $\vec{U}$, defined through

$$\vec{U} = U_1 \hat{e}_x + U_2 \hat{e}_y \qquad (\theta = 0) \qquad (7.1)$$

are related to our fields $\vec{E}_o$, $\vec{E}_2$ by

$$\begin{aligned} b^{-1}U_1 &= E_{ox} - E_{2x} \\ b^{-1}U_2 &= E_{oy} + E_{2y} \end{aligned} \qquad (7.2)$$

This simple relation holds only because Bendow and Gianino have assumed that $\hat{e}_x$ lies in the plane containing the origin ($r'=z=0$), the focal point ($r'=0$, $z=R$) and the field point (r, z). This means that their formula for $\vec{U}$ is restricted to the $\theta=0$ axis. A simple formula for $\theta \neq 0$ involving U_1 and U_2 is possible only for unpolarized, circularly polarized, or linearly polarized light.

For linearly polarized light whose incident polarization makes angle Ψ with the x axis, the diffraction field envelope at (r, $\theta=0$, z) may be written

$$\vec{E} = \begin{bmatrix} (E_o - E_2)\cos\Psi \\ (E_o + E_2)\sin\Psi \end{bmatrix} \tag{7.3}$$

where E_o and E_2, defined beneath eqn. (6.3), are proportional to the incident field amplitude along the polarization direction. In reference 3 , the intensity corresponding to (7.3) is written as

$$|b|^2|\vec{E}|^2 = \cos^2\Psi|U_1(E_x \to E)|^2 + \sin^2\Psi|U_2(E_y \to E)|^2 .$$

For more complicated incident polarization states, eqn. (6.4) must be employed. When the diffraction field is expressed in terms of the fields E_o and E_2, the resulting formulas are usually simpler in appearance, and easier to understand from a physical viewpoint than corresponding formulas based upon U_1 and U_2. We emphasize that E_2 vanishes and E becomes E_o when there is no birefringence. Later we shall discover more physically meaningful differences between E_2 and E_o, and use them to develop our understanding of the influence of birefringence on the transmitted field.

8. General Properties of Radial Dependence of Transmitted Intensity

A. Axial Intensity

All dependence on r or $\rho = r/d$ is contained in the component amplitudes $E_o(\rho, \zeta)$ and $E_2(\rho, \zeta)$ given by (5.5) and (5.6). In these equations ρ appears in the initial phase function, which does not contribute to the intensity, and in the arguments of $J_o(\rho\rho'/\zeta)$ and $J_2(\rho\rho'/\zeta)$. Since $J_2(0) = 0$, the field $E_2(0, \zeta)$ vanishes, and the on-axis field is

$$\vec{E}(0, 0, \zeta) = \vec{E}_o(0, \zeta) \tag{8.1}$$

Thus the axial field has the same polarization as the field incident on the window, even in the presence of birefringence.

At the geometrical focal point, $z=R$, $u=0$, the magnitude of E_o is

$$|E_o(0,\rho)| = \frac{1}{2\pi\rho}\left|\int_0^1 \rho' d\rho' e^{i\phi}\cos\Delta\, E_i(\rho')\right| . \qquad (8.2)$$

Both φ and Δ are functions of ρ' here, and for cylindrical symmetry they are expected to be even functions. One hopes that the phase of E_i is constant, or at least a weak function of ρ', so that the phase variation of the integrand is dominated by φ. If φ and Δ are expanded in powers of ρ',

$$\begin{aligned} \phi &= \phi_o + \phi_2\rho'^2 + \phi_4\rho'^4 + \ldots \\ \Delta &= \Delta_o + \Delta_2\rho'^2 + \Delta_4\rho'^4 + \ldots , \end{aligned} \qquad (8.3)$$

then φ_o contributes a time dependent phase which does not affect the intensity, and $\varphi_2\,\rho^2$ has the same form as the phase introduced by a thin lens of focal length

$$R_\phi = -k/2\phi_2 . \qquad (8.4)$$

This may be positive or negative depending upon the sign of φ_2, and may be removed by adjusting the focal length R. The remaining terms in φ cause spherical aberration, which reduces the focal intensity by an amount depending upon the distribution of the incident intensity in the window aperture. If the aperture is filled uniformly, then the focal intensity is reduced appreciably when $\varphi_4 \approx \pi/2$ (the "Rayleigh limit"[4]). An exact computation for truncated gaussian beams and gaussian aberration is included in a later section.

The lowest order in the expansion of Δ would contribute to the intensity if it were finite, but at the point $\rho'=0$ the window must be isotropic because of the cylindrical symmetry, and thus $\Delta_o=0$. Therefore $\cos\Delta(\rho')$ is unity at the origin, oscillates where Δ is large, at some finite value of ρ', and then returns to unity if the window is isotropic near its periphery. This has the effect of removing annuli from the incident field at the radius where Δ has its maximum value.

The overall result is reduction of the focal intensity by a factor which may oscillate with increasing Δ. A more detailed understanding of the influence of Δ may be gained in the context of particular models, developed in a later section.

At axial points other than the focal point, we expect structure in the intensity whose complexity increases as the aberration increases, and also as the transverse spatial structure of the incident field becomes more abrupt. For example, the axial intensity of a uniformly illuminated aperture, easily found from (8.1) and (5.5), is

$$|\vec{E}(0,0,\zeta)|^2 = \frac{4E_i^2}{\pi u^2 \zeta^2} \sin^2 \tfrac{1}{4}u$$

$$= \frac{4E_i^2}{\pi^2} \frac{\mathcal{R}^2}{(\mathcal{R}-\zeta)^2} \sin^2 \tfrac{1}{4}\left(\frac{1}{\zeta} - \frac{1}{\mathcal{R}}\right) . \qquad (8.5)$$

This has an infinite number of maxima and minima prior to the focal point, and few beyond it. In contrast, the axial intensity of an untruncated gaussian beam, of 1/e intensity radius a, is

$$|\vec{E}(0,0,\zeta')|^2 = \frac{E_i^2}{\pi^2 \zeta'^2 (1 + u'^2)}$$

$$= \frac{E_i^2}{\pi^2 \left[\zeta'^2 + \left(1 - \frac{\zeta'}{\mathcal{R}'}\right)^2\right]} . \qquad (8.6)$$

Here $\zeta' = z/ka^2$, $\mathcal{R}' = R/ka^2$. This is a smooth function with only one maximum at the beam waist. The presence of the abrupt edge at r=d, z=0, in the field of the illuminated aperture is clearly responsible for the violent prefocal oscillations in the transmitted intensity (8.5). In general, increasing truncation

of an otherwise smooth incident intensity distribution causes axial maxima and minima of increasing amplitude prior to the focal region.

B. Off-Axis Intensity

Equations (5.5) and (5.6) for the fields E_o and E_2 are simplest in the geometrical focal plane $z = R$ or $\zeta = \mathcal{R}$:

$$E_o(\rho,\mathcal{R}) = \frac{e^{i\rho^2/2}}{2\pi i\mathcal{R}} \int_0^1 \rho' d\rho' e^{i\phi} \cos\Delta\, J_o(\rho\rho'/\mathcal{R}) E_i(\rho') , \qquad (8.7)$$

$$E_2(\rho,\mathcal{R}) = \frac{e^{i\rho^2/2}}{2\pi i\mathcal{R}} \int_0^1 \rho' d\rho' e^{i\phi} \sin\Delta\, J_2(\rho\rho'/\mathcal{R}) E_i(\rho') . \qquad (8.8)$$

Because J_2 vanishes at zerc argument, E_2 contributes only to the off-axis intensity. In particular, the intensity contribution of E_2 at radius ρ is most strongly influenced by the value of $F \equiv E_i \sin\Delta \exp i\varphi$ at $\rho' \approx 3.1\ \mathcal{R}/\rho = 3.1\ R/kdr$, where J_2 has its first maximum ($J_2(3.1) \approx .486$). Now Δ vanishes at $\rho' = 0$, so $|F|$ possesses a maximum at some finite value $\rho' = \rho'_m$. Therefore, $|E_2|$ is expected to be largest near $\rho_m = 3.1\,\mathcal{R}/\rho'_m$. In many cases Δ is initially zero when the beam first strikes the window, and then increases to a thermal equilibrium value. As Δ increases we expect to see a ring form in the focal plane near ρ_m. The intensity of the ring may oscillate if $\Delta(\rho'_m)$ increases beyond $\pi/2$.

The component E_o tends to have its maximum at $\rho = 0$ when φ and Δ vanish, because J_o has its maximum value at zero argument. The effect of truncation and aberration is as usual to spread the energy over a broader central maximum, and to create subsidiary rings in the focal plane.

In conclusion, we may view the effects of φ and Δ on the focal plane intensity pattern as follows: The initial focal point is near $z = R$, but drifts to larger or smaller values of z, depending upon the sign of $d^2\varphi/dr'^2$, as the mean aberration φ increases. At the same time the axial intensity peak becomes broader and weaker and off axis maxima begin to appear. The

intensity and departure from cylindrical symmetry of this off-axis structure increases with the induced birefringence. The intensity pattern near the axis, where E_0 dominates, is nearly cylindrically symmetric, while the ring associated with E_2 has angular maxima or minima along directions parallel to the major axis of the incident polarization ellipse. Oscillations in the ring intensity and in the axial intensity tend to be out of phase because E_o is proportional to the integral of $\cos\Delta$, and E_2 to the integral of $\sin\Delta$.

9. Aberration Functions for a Simple Window Model

To increase our understanding of the aberration functions φ and Δ, let us compute them for the model analysed extensively by Sparks,[5] Jasperse and Gianino,[6] and Bendow et al.[1] In this model, the window is assumed to be heated by a cylindrically symmetric gaussian beam, and the local temperature is gc erned only by the heating rate, and not affected by thermal diffusion. The window, which is isotropic, expands and develops internal strains as the cooler periphery restricts the expansion of the warmer interior. It is freely supported so the stress vanishes at the window boundary. The two aberration functions Φ_ρ and Φ_θ for this case have been derived by the authors mentioned above, and presented in convenient form by Bendow and Gianino:[1]

$$\Phi_n = C_1^n f(\rho) + C_2^n g(\rho) + C_3^n , \qquad n = \rho,\theta \tag{9.1}$$

Here f and g are functions which depend only upon the incident beam parameters:

$$f(\rho) = \exp -2\alpha^2\rho^2 \tag{9.2}$$

$$g(\rho) = \left[1 - \exp(-2\alpha^2\rho^2)\right]/\alpha^2\rho^2 \tag{9.3}$$

where $2\alpha^2\rho^2 = r^2/a^2$, with a the 1/e intensity radius of the incident gaussian. $\alpha^2 = d^2/2a^2$ is a truncation parameter. The constant phase correction $C_3^o = C_3^\theta$ has no influence on the intensity and is usually suppressed. The remaining constants are functions of the parameters of the medium, and the time integral H(t) of the axial intensity multiplied by the window thickness and an absorption constant:

$$C_1^\rho = H\left\{\frac{\partial n}{\partial T} + \bar{\alpha}(1+\nu)(n-1) + \frac{1}{2}\bar{\alpha}n^3\left[(1-\nu)p_{12} - \nu p_{11}\right]\right\}$$

$$C_1^\theta = H\left\{\frac{\partial n}{\partial T} + \bar{\alpha}(1+\nu)(n-1) + \frac{1}{2}\bar{\alpha}n^3\left[p_{11} - 2\nu p_{12}\right]\right\}$$

$$C_2^\rho = H\left\{\bar{\alpha}n^3(1+\nu)(p_{11}-p_{12})/8\right\} \qquad (9.4)$$

$$C_2^\theta = -C_2^\rho$$

$$H(t) = (\beta w/C')\int^t I_o(t')dt'$$

Here $\partial n/\partial T$ is the rate of change of index with temperature at zero stress, $\bar{\alpha}$ is the coefficient of thermal expansion, ν Poisson's ratio, and p_{ij} the elasto-optic tensor elements. β is the absorption coefficient and C' the specific heat.

With this notation, our aberration functions are

$$\phi = \tfrac{1}{2}k_1(\Phi_\rho + \Phi_\theta)$$

$$= \tfrac{1}{2}k_1(C_1^\rho + C_1^\theta)f(\rho) \qquad (9.5)$$

$$\Delta = k_1 C_2^\rho[g(\rho) - 2f(\rho)] \qquad (9.6)$$

Thus in this formulation each aberration function is proportional to one lumped material parameter, and a function of ρ depending only upon the incident field. If the incident intensity is constant in time, then H(t) is proportional to time, and φ and Δ are proportional to the dimensionless time τ:

$$\phi = \tau f(\rho) \qquad (9.7)$$

$$\Delta = \frac{\sigma\tau}{2}\left[g(\rho) - 2f(\rho)\right] \tag{9.8}$$

where

$$\tau = \tfrac{1}{2}k_1\left(C_1^{\rho} + C_1^{\theta}\right)$$

$$= \frac{\beta k_1 w I_o t}{C'}\left\{\frac{\partial n}{\partial \bar{T}} + \bar{\alpha}(1+\nu)(n-1) + \frac{1}{4}\bar{\alpha}n^3\left[(1-3\nu)p_{12} + (1-\nu)p_{11}\right]\right\} \tag{9.9}$$

and

$$\sigma = 4C_2^{\rho}\Big/\left[C_1^{\rho} + C_1^{\theta}\right] . \tag{9.10}$$

It is important to notice that in this formulation, the introduction of birefringence, $p_{11} \neq p_{12}$, requires the introduction of only one additional material parameter σ into the equations in the context of the model most frequently used to estimate the influence of birefringence. The value of σ may be inferred easily from the ratios C_2^{ρ}/C_1^{ρ}, C_1^{θ}/C_1^{ρ} tabulated by Bendow and Gianino[1], and is shown in Table (9.1) for the materials they considered.

Now let us examine the functional dependence of Δ and φ upon ρ. Figure (9.1) shows f and $\frac{1}{2}(g-2f)$ plotted on the same scale. The function $\Delta/\sigma\tau$ reaches its maximum value of .298 at r/a = 1.34 where $\emptyset/\tau$ has declined to .167. This means that the birefringence is largest in the low intensity wings.

With these expressions for the aberration functions φ and Δ, we shall analyse the following problem: given a particular incident beam truncation parameter, for what value of the material parameter σ does birefringence begin to play an important role in reducing the focal intensity? To this end, we first determine the focal intensity without birefringence.

10. Focal Intensity with No Birefringence for Simple Window Model

Taking Δ=0, we find the focal field

$$\left|\vec{E}(0,\rho)\right| = \frac{E_i}{2\pi\rho}\left|\int_0^1 \rho' d\rho' \exp\left[i\tau\exp(-2\alpha^2\rho'^2)\right]\exp -\alpha^2\rho'^2\right| \tag{10.1}$$

Table 9.1 Dimensionless Times and Birefringence Parameters

(Based on values tabulated in Ref. 1)

Material	σ	$\tau / w \int^{t} I_o(t')dt'$
KBr	- .598	- 0.14
KCℓ	-1.344	- 2.51
NaCℓ	-0.202	- 6.30
KI	-0.296	- 7.91
CsI	0?	- 63.6
CsBr	0?	- 80.7
CdTe	.0317	-181.4
KRS-5	0?	588.
ZnSe	.0746	1424.
GaAs	- .00886	2990.
InSb	0?	9790.
Ge	.0139	8570.
TI Glass# 1173	0?	2890.
TI Glass# 20	0?	3780.
Irtran-4 (ZnSe)	.0829	4310.
Irtran-6 (CdTe)	.0423	19500.

w = window thickness (cm)

I_o = incident axial intensity (Watt/cm^2)

t = time since turn-on (sec.)

σ and τ are dimensionless

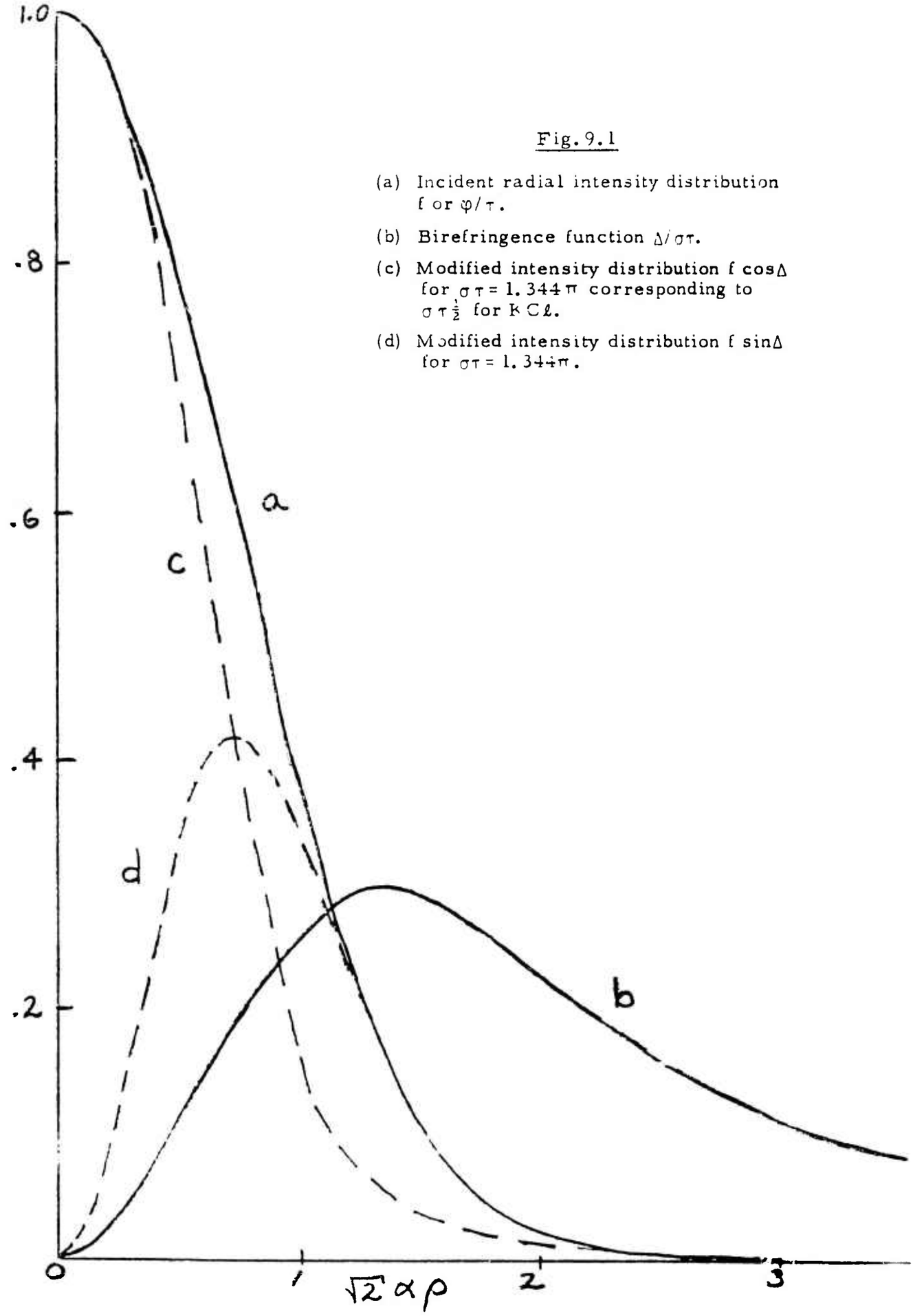

Fig. 9.1

(a) Incident radial intensity distribution f or φ/τ.

(b) Birefringence function $\Delta/\sigma\tau$.

(c) Modified intensity distribution f cosΔ for $\sigma\tau = 1.344\pi$ corresponding to $\sigma\tau\frac{1}{2}$ for K C ℓ.

(d) Modified intensity distribution f sinΔ for $\sigma\tau = 1.344\pi$.

where the incident field is

$$E_i(\rho') = E_i \exp - \alpha^2 \rho'^2 \tag{10.2}$$

As we have shown elsewhere[7], this integral can be evaluated exactly in terms of Fresnel functions, which can be easily visualized with the aid of Cornu's spiral. The result for the focal intensity is

$$|\vec{E}(0,\rho)|^2 = \frac{E_i^2}{4\pi^2\rho^2} \frac{1}{4\alpha^4\tau} \left| \int_{\tau^{\frac{1}{2}}}^{\tau^{\frac{1}{2}}} e^{-\alpha^2} \, dy e^{iy^2} \right|^2$$

$$= \frac{E_i^2}{16\pi^2\alpha^4\rho^2} \left(\frac{\pi}{2\tau}\right) \left\{ \left[C(\sqrt{2h\tau}/\pi) - C(\sqrt{2\tau}/\pi) \right]^2 \right.$$

$$\left. + \left[S(\sqrt{2h\tau}/\pi) - S(\sqrt{2\tau}/\pi) \right]^2 \right\} \tag{10.3}$$

Here $h \equiv \exp -2\alpha^2$, and S(u), C(u) are the Fresnel sine and cosine integrals which give the y and x coordinates, respectively, of a point on the Cornu spiral. The argument u measures the arc length along the spiral from the origin to the point [C(u), S(u)].

In the absence of thermal distortion ($\tau = 0$) the focal intensity becomes

$$I_R = \frac{P_o k^2 a^2 (1 - h^{\frac{1}{2}})^2}{\pi R^2} \tag{10.4}$$

where P_o is the total power in the incident gaussian beam, and a is the 1/e intensity radius. This function has a maximum, if regarded as a function of a for fixed d, when h= 0.0805, or a = 0.63d. That is, this choice of truncation maximizes the focal intensity for fixed beam power and window size, and provides a useful reference point for the truncation parameter.

For the optimum value h = 0.0805, evaluation of eqn. (10.3) shows that the focal intensity drops to half its aberrationless value when $\tau = \tau_{\frac{1}{2}} \equiv 0.965\,\pi$. This characteristic degradation time is very close to that estimated by Jasperse and Gianino[6], who analysed this model using geometrical optics. We shall set $\tau_{\frac{1}{2}} = \pi$ for convenience in subsequent sections.

The remainder of this analysis will be included in the next quarterly report. The new results reported here may be summarized as follows: The analysis of thermal lensing based upon the elementary fields $\vec{E}_o$ and $\vec{E}_2$ leads to simple formulas for the azimuthal dependence of the transmitted field intensity and polarization state for an arbitrary incident polarization state. It also clearly separates the effect of birefringence from the "scalar" refocusing and aberration phenomena. Furthermore, it allows the influence of birefringence to be characterized by a single material parameter σ rather than the two parameters C_2^o/C_1^ρ and C_1^θ/C_1^ρ necessary in the formulation of Bendow and Gianino. This allows vast simplification both in the development of the theory, and in the presentation of data. It also provides an intuitive basis for the much more complicated non-cylindrically symmetric theory to be presented in future reports.

References

1. B. Bendow, P. D. Gianino "Theory of On-Axis Intensity Distribution in Thermal Lensing" (LQ-10 High Power Laser Window Program) AFCRL 72-0322, Physical Sciences Research Paper No. 494, (1972)
2. M. Born, E. Wolf "Principles of Optics" 4th Edition, Pergamon Press (1970)
3. 'High Power Infrared Laser Materials" (LQ-10 Program) Quarterly Progress Report No. 3 AFCRL-71-0568, Special Report No. 125
4. R. K. Luneberg, "Mathematical Theory of Optics" Univ. of California Press (1966) (Page 341)
5. M. Sparks, J. Appl. Phys. 42, 5029 (1971)
6. J. R. Jasperse, P. D. Gianino, J. Appl. Phys. 43, 1686 (1972)
7. J. Marburger, M. Flannery, Conference on High Power Infrared Laser Window Materials AFCRL-71-0592, Special Report No. 127, p. 11 (1971)

DISCUSSION

The lowest absorption at 10.6μm found with melt grown GaAs remains at $8 \times 10^{-3}cm^{-1}$. It has now been established that the weak temperature dependence of this absorption fits the predictions of theory for multi phonon absorption, supporting the view that the mentioned value represents the theoretical limit. However, this conclusion is not completely final. Weak temperature dependencies may also result from other mechanisms. An increase of the IR absorption spectrum after heating at 400°C with maintenance of the wavelength dependence seems to indicate that defects are still involved. Attempts to grow GaAs by a completely different method - chemical vapor transport - have been partly successful. Layers up to 2mm in thickness were obtained. Unfortunately, the layers contain inclusions, and the relatively high 10.6μm absorption measured with these layers is probably due to these. In the next contract period we shall concentrate on growing from Ga(ℓ); these will probably be of better quality and will enable us to finally decide whether GaAs is a serious contender as a window material.

An electrochemical method was developed to measure oxygen in Ga(ℓ). By dissolving GaAs in this liquid, the oxygen content of the GaAs can be determined. Oxygen at a level of $10^{18}cm^{-3}$ was found in a Te-doped crystal. No O was found in an Si-doped crystal, grown in oxygen rich environment. It is believed that this is due to the stability of SiO_2. The oxygen present in a concentration < 2 × that of Si is not detected by our method.

Structural investigations on Silicon-doped GaAs indicate that hardening occurs in the presence of tetragonal defects. Deformation studies show that slip in GaAs occurs on only one system: $\{111\}\langle 1\bar{1}0\rangle$. Diffraction patterns show diffuse streaks which are attributed to diffuse scattering of electrons at acoustic phonons.

In repeating dielectric constant measurements, it was found that a considerable inaccuracy arises from errors in the measurement of the sample thickness and area, and in lack of flatness. The best value found so far is $\varepsilon = 13.6$, larger than the value first reported. Further refinements are being made.

Crystals of KBr were grown which showed an absorption at 10.6μm of $1.1 \times 10^{-3}cm^{-1}$, far above what theory predicts. $KBrO_3$ has been suggested as

the possible cause of this absorption.

Attempts to prepare dense polycrystalline ingots of CdTe by hot-pressing in the presence of an excess of cadmium still are not completely successful.

We are presently remeasuring the high-temperature Hall effect on CdTe, and will compare the result with those of measurements made on cooled cyrstals in order to see what changes, if any, occur during cooling. Comparison of our high-temperature data on indium-doped CdTe and published data on cooled crystals indicate that native donors (probably interstitial Cd) precipitate.

Multiphonon absorption may be due to anharmonic forces and/or to a non-linear dependence of ionic dipoles or in displacement. An experimental method to determine the ratio in which the two mechanisms contribute is proposed. The theory of thermal lensing is being reviewed and is being reformulated based on considering the effect from a different viewpoint.